Journal of Petroleum Science and Engineering 221 (2023) 111309

Contents lists available at ScienceDirect

Journal of Petroleum Science and Engineering

journal homepage: www.elsevier.com/locate/petrol

Pore throat heterogeneity of different lithofacies and diagenetic effects in gravelly braided river deposits: Implications for understanding the formation process of high-quality reservoirs

Dingding Zhao [a,b], Jiagen Hou [a,b,*], Hemanta Sarma [c], Wenjie Guo [d], Yuming Liu [a,b,**], Pengfei Xie [a,b,***], Luxing Dou [e], Ruxian Chen [a,b], Zhanyang Zhang [f]

[a] State Key Laboratory of Petroleum Resources and Prospecting, China University of Petroleum-Beijing, Beijing, 102249, China
[b] College of Geosciences, China University of Petroleum-Beijing, Beijing, 102249, China
[c] Department of Chemical and Petroleum Engineering, University of Calgary, Calgary, T2N 1N4, Canada
[d] The Second Oil Production Plant of PetroChina Changqing Oilfield Company, Qingyang, Gansu, 745000, China
[e] College of Resources and Environment, Yangtze University, Wuhan, 430100, China
[f] Exploration and Development Research Institute, SINOPEC North China Company, Zhengzhou, Henan, 450006, China

ARTICLE INFO

Keywords:
Tight sandstone gas reservoir
Lithofacies
Pore throat structure
Fractal characteristic
Diagenesis
Ordos basin

ABSTRACT

Tight gas sandstone is a unique kind of unconventional hydrocarbon resource in that its intricate pore throat structure governs reservoir physical properties and gas reservoir productivity. However, the effect of differential diagenesis of various lithofacies on the heterogeneity of pore throat structure remains unclear. In this paper, a series of experiments were integrated to evaluate pore throat structures and fractal characteristics of the different lithofacies in a tight sandstone gas reservoir, and followed by a study of the impact of diagenetic alteration on them. Results demonstrate that the mineral composition, dominant pore types, pore throat structural parameters, fractal dimension, and physical properties of various lithofacies are notably different, which is mostly attributable to diagenetic alteration variability. There are more primary pores and less clay mineral content in coarser lithofacies. Pebbly coarse-grained sandstone and sandy conglomerate reservoirs that have undergone strong dissolution have more composite pores composed of residual intergranular pores and dissolution pores, which help to form a homogeneous pore throat system with good connectivity, resulting in the best reservoir quality. Due to the strong compaction and high clay mineral content filling pores and throats in medium-grained sandstone and fine-grained sandstone lithofacies, a large number of primary pores were lost, and throats were blocked, which easily formed intercrystalline pores, leading to poor reservoir quality. Coarse-grained sandstone reservoirs with moderate clay mineral content have undergone moderate compaction and dissolution and have moderate reservoir quality. Filamentous illite is the most destructive clay mineral to pore throat connectivity. Intergranular dissolution pores and moldic pores contribute significantly to the physical properties of pebbly coarse-grained sandstone and sandy conglomerate reservoirs. Pebbly coarse-grained sandstone and sandy conglomerate lithofacies are considered high-quality reservoirs with greater development potential for tight gas. This work has important guiding significance for the prediction of high-quality reservoirs in similar tight sandstone reservoirs.

1. Introduction

Global production of tight sandstone gas has rapidly risen over the past few decades (Rezaee et al., 2012; Jia et al., 2021). Tight sandstone gas has an ever-increasing role in energy consumption and is an important source of clean energy around the globe (Dai et al., 2012; Zou et al., 2013, 2018; Misiak et al., 2014). The reservoir formed by gravelly braided river deposits is an important type of tight sandstone gas

* Corresponding author. College of Geosciences, China University of Petroleum-Beijing, No. 18, Fuxue Road, Changping District, Beijing, 102249. China.
** Corresponding author. College of Geosciences, China University of Petroleum-Beijing, No. 18, Fuxue Road, Changping District, Beijing, 102249. China.
*** Corresponding author. College of Geosciences, China University of Petroleum-Beijing, No. 18, Fuxue Road, Changping District, Beijing, 102249. China.
E-mail addresses: jghou63@hotmail.com (J. Hou), liuym@cup.edu.cn (Y. Liu), 284023229@qq.com (P. Xie).

https://doi.org/10.1016/j.petrol.2022.111309
Received 25 July 2022; Received in revised form 6 November 2022; Accepted 30 November 2022
Available online 14 December 2022

reservoir, which is widely dispersed throughout the world (Miall, 1977; Lunt and Bridge, 2004; Sun et al., 2019; Huang et al., 2020a; Li et al., 2020a; Zhang et al., 2020).

The sedimentary environment of the gravelly braided river is characterized by strong hydrodynamic conditions, which can form large-area superimposed sand bodies (Bluck, 1979; Lunt and Bridge, 2004; Wang et al., 2021a). The complicated lithofacies type, a high degree of heterogeneity, and complex pore structure of these reservoirs make it challenging to predict high-quality reservoirs with good physical properties (Tobin et al., 2010; Tong et al., 2012; Stroker et al., 2013; Wang et al., 2021b). Lithofacies classification based on petrological characteristics is an efficient method for characterizing reservoirs. Mineral composition, grain size, sedimentary texture, physical properties, microscopic pore throat features, diagenesis types, and intensity vary significantly between lithofacies (Heward, 1989; Arnott et al., 2003; Ebinghaus et al., 2012; Wilson et al., 2020; Feng et al., 2021; Cao et al., 2021; Yang et al., 2022). Varied lithofacies have different reservoir quality evolution processes. The lithofacies categorization is helpful in analyzing the interaction between physical attributes, pore structure, and diagenesis heterogeneity of tight sandstone gas reservoirs (De Ros and Goldberg, 2007; Aliyev et al., 2016; Oluwadebi et al., 2018; Mehrabi et al., 2019; Xiao et al., 2020; Wang et al., 2020a; Wang et al., 2020b; Cao et al., 2021). The extremely poor reservoir quality of tight gas sandstone is the result of complicated and intense diagenetic alteration (Cant and Ethier, 1984; Ehrenberg, 1989; Wang et al., 2019; Yu et al., 2019; Li et al., 2020b; Qiao et al., 2020a; Wheatley et al., 2020). Different lithofacies undergo distinct diagenetic evolution processes, resulting in distinct pore structures, according to several studies (Mehrabi et al., 2019; Cao et al., 2021; Yang et al., 2022).

Although there have been many studies on the pore structure, fractal characteristics, and diagenesis of tight sandstone reservoirs, the majority of them are focused on fine-grained sediment reservoirs and are primarily limited to samples with various sedimentary microfacies or physical properties (Lai et al., 2018a; Guo et al., 2019; Wang et al., 2019; Qiao et al., 2020b, 2021; Huang et al., 2020b; Qu et al., 2020; Yin et al., 2020). However, little is known about how the complex diagenetic alteration of distinct lithofacies in gravelly braided river deposits impacts the pore structure heterogeneity.

The Dongsheng Gas Field is a giant gas field with 100 billion m^3 of reserves discovered in recent years by SINOPEC in the northern Ordos Basin (He et al., 2020). Previous studies focused on the Sulige, Yulin, and Daniudi gas fields in the Ordos Basin (Dai et al., 2012; Liu et al., 2015; Fan et al., 2019; Qiao et al., 2019), but there has been little research conducted on the Dongsheng Gas Field. An in-depth investigation into the pore structure and the effect of diagenetic alteration on it of gravelly braided river deposits is favorable for predicting a high-quality reservoir and efficiently developing the gas field, and it also serves as a significant reference for other tight sandstone gas reservoirs around the world. Taking the Lower Shihezi formation reservoir in the X block of Dongsheng Gas Field as an example, this study integrates several experimental techniques, including casting thin section (CTS), scanning electron microscopy (SEM), X-ray computerized tomography (X-CT), high-pressure mercury intrusion (HPMI), nuclear magnetic resonance (NMR), and X-ray diffraction (XRD), to examine the pore structure and fractal properties, as well as the effect of diagenesis on the microscopic pore structure heterogeneity of various lithofacies in tight gas sandstone. The primary goals of this study are as follows: (1) to investigate the petrological and physical properties characteristics of distinct lithofacies; (2) to comprehensively characterize the size, morphology, and connectivity of pores and throats in different lithofacies; (3) to use NMR to characterize the fractal characteristics of pore structure and to clarify the correlation between fractal dimension, microstructural parameters, and physical properties, and (4) to determine the effect of diagenetic modification on the heterogeneity of pore throat structure in various lithofacies.

2. Geological background

The Ordos Basin, which was formed on the North China Platform (Fig. 1A), is a multi-cycle craton basin and the second biggest sedimentary basin in inland China, with an area of about 25×10^4 km^2 (Yang et al., 2005; Xiao et al., 2005). The basin encompasses six major tectonic parts, including the Weibei Uplift, Yimeng Uplift, Jinxi Folding Belt, Western Thrusting Belt, Yishan Slope, and Tianhuan Depression (Fig. 1B) (Yang et al., 2000). The Dongsheng Gas Field is located on the southern margin of the Yimeng Uplift, and it has three near east-west faults: Porjianghaizi fault, Wulanjilinmiao fault, and Sanyanjing fault (Fig. 1B). The study region is in the X block, which lies in the center and south of the Dongsheng Gas Field and covers around 800 km^2. The Porjianghaizi fault is situated at the northern edge of the X Block (Fig. 1C). It is a northward thrust fault that stretches for about 70 km, and the target layer's fault distance is 300 m (Xu et al., 2018).

The strata of the Upper Paleozoic Permian in Dongsheng Gas Field are the Taiyuan, Shanxi, Lower Shihezi, Upper Shihezi, and Shiqianfeng formation from lowest to highest (Fig. 2). The principal production horizon in the study region is the Lower Shihezi formation, which can be separated into He-1, He-2, and He-3 Members. The target layer is buried to a depth of 3100–3300 m, and it has a small dip angle and relatively flat strata. The sedimentary environment is a gravelly braided river system, primarily composed of the braided channel, braided bar, and floodplain sediments. The reservoir is dominated by pebbly coarse-grained clastic rock (Wang et al., 2014, 2020a; Li et al., 2021). The coal seams and dark mudstone of the Shanxi and Taiyuan formations are the primary source rocks, supplying abundant natural gas for the overlying Lower Shihezi formation (Xiao et al., 2005; Xu et al., 2018). The vitrinite reflectance (R_o) of source rocks ranges between 1.16% and 1.35%, with a mean value of 1.25%. The total organic carbon content (TOC) ranged between 32.5% and 70.0%, with a mean value of 58.5%. The maximum pyrolysis temperature (T_{max}) ranges between 462 °C and 477 °C, with a mean value of 466 °C. The hydrocarbon generation potential (S_1+S_2) ranges between 42 mg/g and 123.14 mg/g, with a mean value of 103.62 mg/g. The chloroform bitumen "A" ranges between 0.39% and 2.16%, with a mean value of 0.96%. The coal-bearing source rocks have entered the mature and high maturity stages (Dai et al., 2005; Xiao et al., 2005). The thick, widely distributed mudstone of the Upper Shihezi formation is an effective capping rock.

3. Samples and methodology

3.1. Sample information and experiment process

The study gathered 32 cylindrical sandstone samples from the target layer of 20 exploration wells in the X block of the Dongsheng Gas Field, which contained the vast majority of reservoir lithofacies types. Each sample measuring 2.5 cm in diameter and 8 cm in length was obtained by perpendicularly drilling fresh core plugs from the wellbore. In addition, porosity and permeability data of 156 samples, CTS analyses of 195 samples, SEM data of 14 samples, and cathode luminescence (CL) data of 19 samples were collected from SINOPEC North China Company. Before the experiment, 32 samples were washed, the residual hydrocarbons were removed, and then dried for 48 h at 120 °C. Initially, their porosity and permeability were tested. After that, the top of each sample was cut out with a length of 0.5 cm for observation of CTS to investigate the petrological characteristics, pore morphology, and genetic types of different samples. On the basis of the assessment of physical properties and CTS, eight representative samples of various lithofacies were selected for the combination experiment. These eight representative samples were taken from the channel bar sedimentary microfacies.

Eight representative samples were cut into 2.5 cm and 5 cm parts. First, five samples were selected from the 2.5 cm part of the eight samples with different lithofacies for X-CT analysis, and then the 2.5 cm part of the eight samples was observed by SEM. At the same time, an

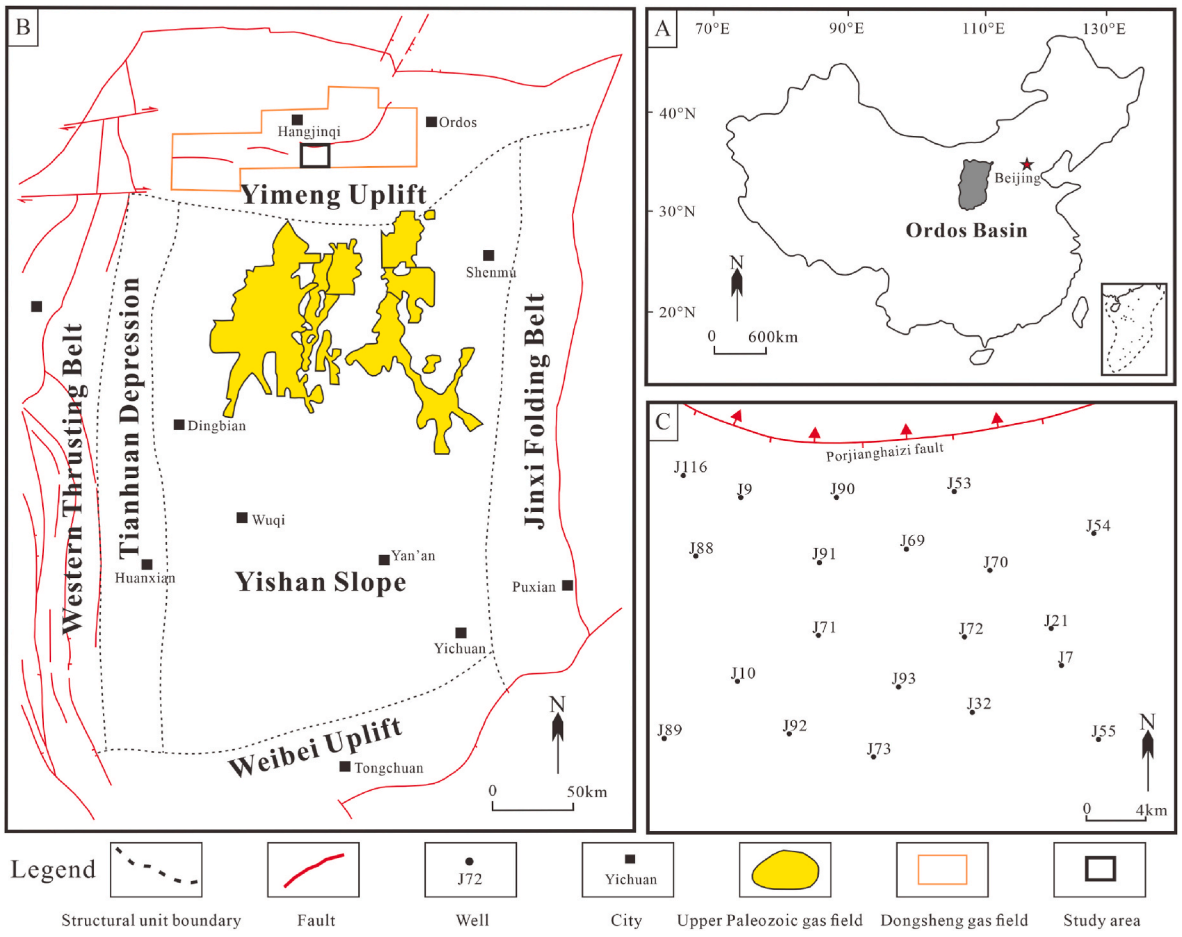

Fig. 1. Location map of the Ordos Basin in China's map (A); The structural position map of the X block in the Ordos Basin (B); Locations of exploration wells and Porjianghaizi fault in the X block (C) (modified from Yang et al., 2012; Wang et al., 2020a; Qin et al., 2022).

NMR test was conducted on the 5 cm part of eight samples, and then after drying, the 5 cm part was cut into 2 cm and 3 cm parts. The 3 cm part was used for the HPMI test, and the 2 cm part was used for bulk XRD analysis. Details of each experiment involved are described below.

3.2. Experiments

3.2.1. Porosity and permeability

A CMS-300 apparatus was used to test porosity and permeability at the State Key Laboratory of China University of Petroleum-Beijing (CUPB). The helium dilation method and the dynamic pressure method were used to measure porosity and permeability, respectively. Klinkenberg calibration was performed during the permeability measurement, which was performed at the ambient temperature of 25 °C and the confining pressure of 200 psi by SY/T 5336–2006. The porosity and permeability measured in experiments are commonly referred to as effective porosity and absolute permeability.

3.2.2. CTS and SEM

The polished thin sections with a thickness of 0.3 mm were impregnated with blue resin and analyzed with a Nikon-LV100nPOL polarizing microscope. The rock composition, pore and throat type, morphology, particle sorting, grinding, and cementation of sandstone samples were studied by the point counting method. Generally, at least 200 points were quantified for each sample. The statistical error of each micrograph was less than 2%. The test standard is SY/T 5368–2016. The polished and golden-coated thin slices were used for SEM analysis using the Quanta-200 F FESEM with the highest resolution of 1.2 nm. SEM analysis can obtain high-resolution microscopic images of pores and throats, authigenic minerals, and intercrystalline micropores of clay minerals at nano-to micro-scale and further study mineral paragenetic sequences, clay mineral morphology, pore size, and connectivity.

3.2.3. X-CT

Five tight sandstone samples with varying lithofacies were analyzed using X-CT. The cylinder samples were around 5 mm in diameter and length. The size, connectivity, and heterogeneity of complex pore-throat networks can be visually characterized using this technique. The experiment was conducted on the Zeiss Xradia versa-510 Micro-CT instruments of the State Key Laboratory of CUPB, which were set with 100 Kv voltage and 90 μA current, a resolution of 3 μm, and an exposure time of 2.0 s under conditions of 20 °C ambient temperature and 40% relative humidity. It ensures X-ray penetration of tight sandstone samples and good imaging. The Zeiss reconstruction software was used to reconstruct the 3D grayscale image after the original 2D grayscale tomography data was obtained. FEI Avizo 9.0.1 was further used to segment the reconstructed images to obtain the pore system of the sandstone sample. The maximum sphere algorithm-based pore network model can effectively identify the pores and throats and calculate detailed pore structure geometry parameters. The detailed data processing process of this method is completely elaborated by Dong and Blunt (2009).

3.2.4. NMR

The transverse relaxation time (T_2) spectrum obtained by NMR experiments can provide quantitative information for pores of all sizes. The Recore-04 low-field NMR spectrometer is employed for the NMR

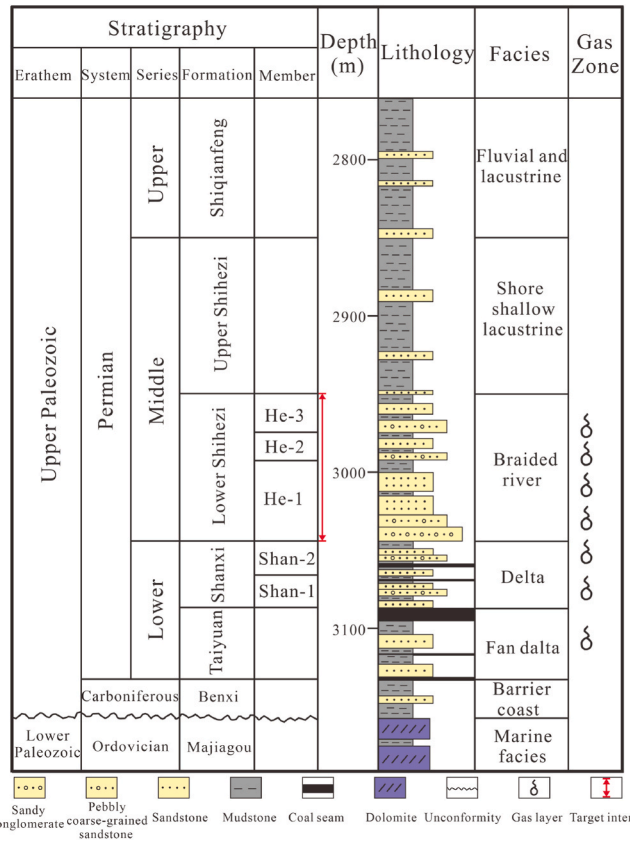

Fig. 2. The stratigraphy column of the Permian System in Dongsheng Gas Field, Ordos Basin (modified from Zheng et al., 2020; Li et al., 2021).

examination of eight cylindrical samples of varying lithofacies, each measuring around 2.5 cm in diameter and 5.0 cm in length. The experiment followed the Chinese test standard SY/T 6490–2014, set the resonance frequency as 2.38 Mhz, echo interval and echo number as 0.1 ms and 17,500, respectively, waiting time as 3 s, scanning times as 32, and it was carried out at 20 °C and 40% relative humidity. These samples were dried at 120 °C for 24 h before being vacuumed and saturated with simulated formation water with a salinity of 41,714 mg/L, which is equivalent to the salinity of formation water in the Lower Shihezi formation. A first NMR test was performed on the fully saturated water sample, which was subsequently centrifuged in a high-speed centrifuge for 1 h at 400 psi centrifugal pressure, followed by a second NMR test on the centrifuged sample. The Carr-Purcell-Meiboom-Gill (CPMG) sequence was used to acquire the T_2 spectrum of the fully saturated water and 400 psi centrifuged samples. The T_2 spectrum of each sample can be converted into pore radius by the formula $T_2 = \frac{1}{\rho} \bullet \frac{r}{c}$ (Mao et al., 2005; Saidian and Prasad, 2015; Daigle and Johnson, 2016), where ρ, r, and c are the surface relaxation rate, pore radius, and shape factor, respectively ($c = 3$ in sphere pores and $c = 2$ in cylinder pores). In this study, the c value is 2, and the pores of tight sandstone samples obtained by NMR are considered cylindrical.

3.2.5. HPMI

The HPMI experiment was conducted with an AutoPore IV9505 mercury porosimeter at the Chinese Academy of Sciences' Institute of Hydrodynamics and Fluid Mechanics in Langfang, China. The test standard is according to Chinese standard SY/T 5346–2005. The eight cylindrical samples had a diameter of 2.5 cm and a length of 3.0 cm. The highest mercury intrusion pressure was set to 200.62 MPa, and the corresponding pore radius was 0.0037 μm, which was the smallest pore radius obtained in the test. After the mercury injection pressure reaches the maximum, the pressure progressively declines and the mercury is withdrawn from the sample. The HPMI test can acquire the capillary pressure vs. mercury saturation curve during mercury intrusion and extrusion. The equivalent pore throat radius of capillary pressure can be computed using the Washburn equation. Finally, multiple characteristic parameters representing pore size distribution can be obtained.

3.2.6. XRD

The X-ray diffraction patterns of different mineral crystals are distinct. The mineral content of the sample is positively correlated with its characteristic peak intensity in the spectrum. The content of different minerals can be determined using the "K value method". Tight sandstone samples were crushed and ground into nearly 200 mesh powders. This experiment was conducted on the samples using the D8 DISCOVER X-ray diffractometer to obtain quantitative data on mineral composition and various clay mineral kinds. Random powder mounts of bulk samples were measured in a step scan mode from 2 to 65° 2θ with a step increment of 0.01 2θ and a count time of 0.3 s per step (Haile et al., 2018). The ambient temperature and humidity were set at 27 °C and 22%, respectively. The test method and procedure follow the national standard SY/T5163-2018.

3.3. Fractal dimensions

Based on the fractal principle, the number of pores having a pore radius greater than r-N(>r) in a reservoir with a fractal pore feature is a function of pore radius and can be described as follows (Mandelbrot, 1975; Zhang et al., 2007; Daigle et al., 2014; Lai et al., 2018b):

$$N(>r) = \int_{r}^{r_{max}} P(r)dr = ar^{-D} \tag{1}$$

where r_{max}, P(r), D, and a are the maximum pore radius, pore radius distribution density function, fractal dimension, and the proportionality constant of the reservoir, respectively.

Taking the derivative of both sides of Eq. (1) with regard to r, and obtain:

$$P(r) = \frac{dN(>r)}{dr} = br^{-D-1} \tag{2}$$

Where $b = -Da$, b is proportionality constant.

Based on Eq. (2), the cumulative pore volume with pore radius less than r in the reservoir can be described as follows:

$$V(<r) = \int_{r_{min}}^{r} P(r)mr^3dr = m'\left(r^{3-D} - r_{min}^{3-D}\right) \tag{3}$$

where r_{min} is the minimum pore radius, and m is a parameter associated with pore shape (m = 1 in cubic pores, m = π in cylinder pores, and m = 4π/3 in sphere pores).

According to Eq. (3), considering $r_{max} \gg r_{min}$, the formula for accumulated pore volume fraction S_V with pore radius less than r in the reservoir can be described as

$$S_V = \frac{r^{3-D} - r_{min}^{3-D}}{r_{max}^{3-D} - r_{min}^{3-D}} = \left(\frac{r}{r_{max}}\right)^{3-D} \tag{4}$$

According to the formula $T_2 = \frac{1}{\rho} \bullet \frac{r}{c}$, Eq. (4) can be converted into

$$S_V = \left(\frac{T_2}{T_{2\,max}}\right)^{3-D} \tag{5}$$

Taking logarithms for both sides of Eq. (5):

$$\lg(S_V) = (3-D)\lg(T_2) - (3-D)\lg(T_{2\,max}) \tag{6}$$

Consequently, the fractal dimension can be calculated through T_2

spectrum data obtained by the NMR experiment. By drawing the relationship curve between $lg(S_V)$ and $lg(T_2)$, the curve slope K was obtained, and the fractal dimension D = 3-K was further obtained (Lai and Wang, 2015; Zhu et al., 2018; Qiao et al., 2021).

4. Results

4.1. Lithofacies characteristics and mineral compositions

According to the observation of the 382.52 m cores from the Lower Shihezi formation, it is evident that the sandstone is primarily massive. Five lithofacies types were defined depending on grain size and gravel content, namely sandy conglomerate (Sc), pebbly coarse-grained sandstone (Ps), coarse-grained sandstone (Cs), medium-grained sandstone (Ms), and fine-grained sandstone (Fs) (Fig. 3). The diameter of gravel in Sc reservoirs ranges from 2 mm to 32 mm. The gravel is moderately rounded and poorly sorted. The diameter of gravel in Ps reservoirs ranges from 2 mm to 25 mm, and is well-rounded and poorly sorted. Cs, Ms, and Fs reservoirs have good sorting and are rounded. Parallel bedding can be seen in the Fs reservoirs. Different lithofacies have undergone distinct diagenetic evolution processes, resulting in distinct pore structures and physical properties.

According to CTS data and Folk's classification scheme (Folk et al., 1970), the predominant rock types of the Lower Shihezi formation are sublitharenite and litharenite, with a small amount of feldspathic litharenite and quartz arenite (Fig. 4). The rock fragments are mostly metamorphic, with a minor quantity of igneous and sedimentary rock. The sandstone grains are moderately sorted and subangular to

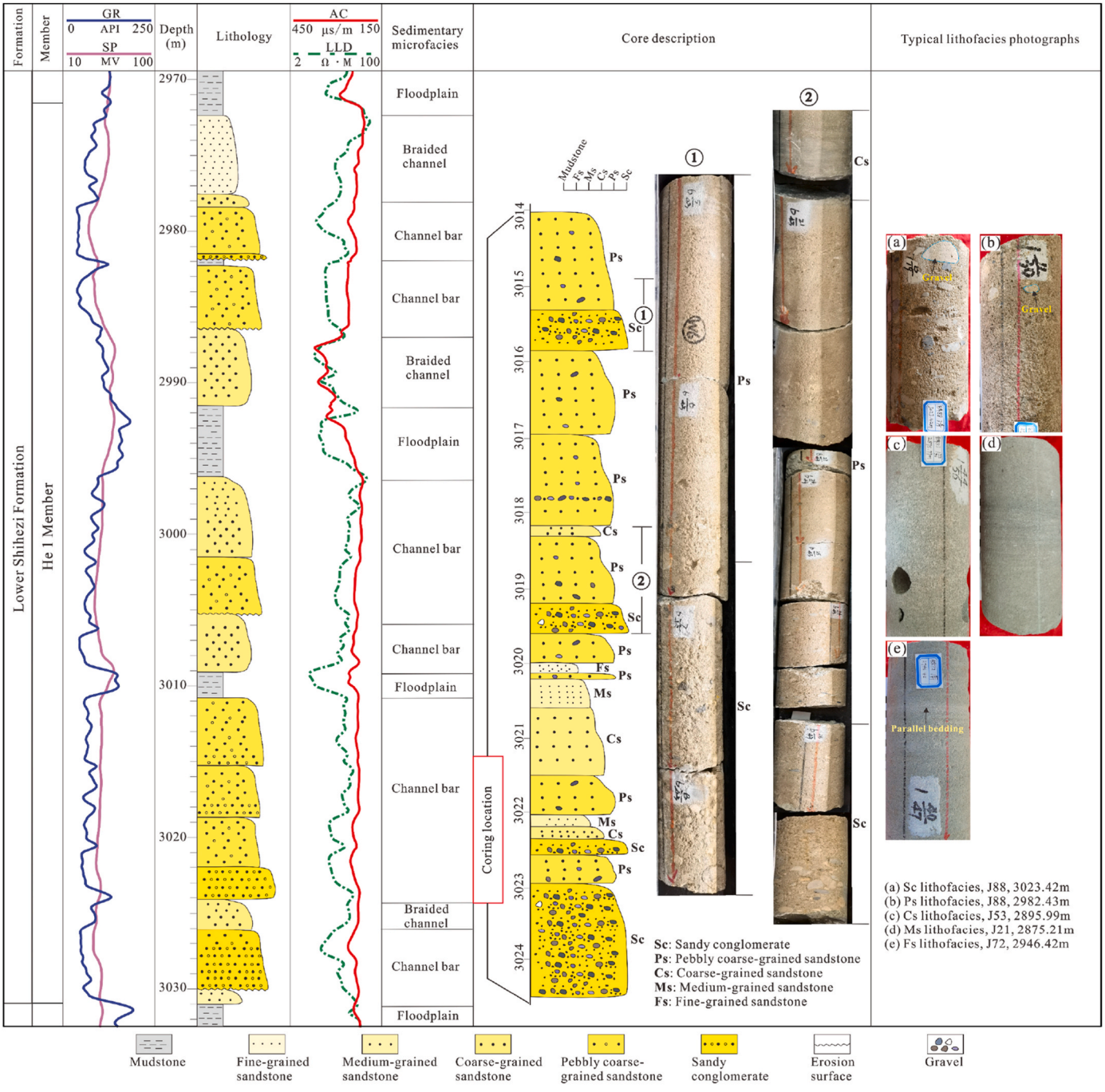

Fig. 3. Sedimentary microfacies interpretation and lithofacies description of well J88, and typical lithofacies photographs from different wells.

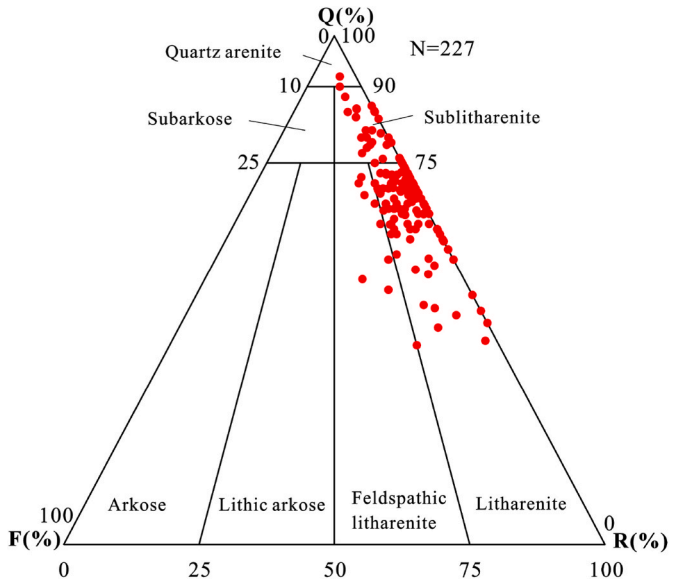

Fig. 4. Quartz(Q)-feldspar(F)-rock fragment(R) ternary plot showing the grain composition of the Lower Shihezi formation sandstones (classification after Folk et al., 1970).

subrounded. The cements of sandstone reservoirs are mainly clay minerals and calcite. The results of bulk XRD analysis (Fig. 5) (Table 1) show that quartz is the mineral with the highest content in all samples, with a mean value of 78.3%. The absolute content of clay minerals ranges between 9.6% and 26.2%, with a mean value of 17.7%. The feldspar and calcite content is low, with a mean value of 0.8% and 3.0%, respectively. Moreover, there are small amounts of dolomite, szaskaite, and analcime in some samples. The average absolute total clay mineral content of Sc, Ps, Cs, Ms, and Fs lithofacies is 15.3%, 9.9%, 17.9%, 19.9%, and 24.4%, respectively (Table 1). With the decrease in particle size, the clay mineral content increases. The highest clay mineral content is found in Fs lithofacies. Clay minerals are mostly composed of kaolinite, illite, chlorite, and illite/smectite mixed layer, with average absolute contents of 5.175%, 4.959%, 3.743%, and 3.811%, respectively (Table 1). Kaolinite is the most abundant of all clay minerals.

4.2. Physical properties

The porosity of 188 tight sandstone samples ranges between 0.8% and 19.3%, with a mean value of 8.6%, and the permeability ranges between 0.012 mD and 6.47 mD, with a mean value of 0.660 mD. The samples with porosity less than 10% and permeability less than 1mD accounted for 55% of the total samples. Porosity and permeability

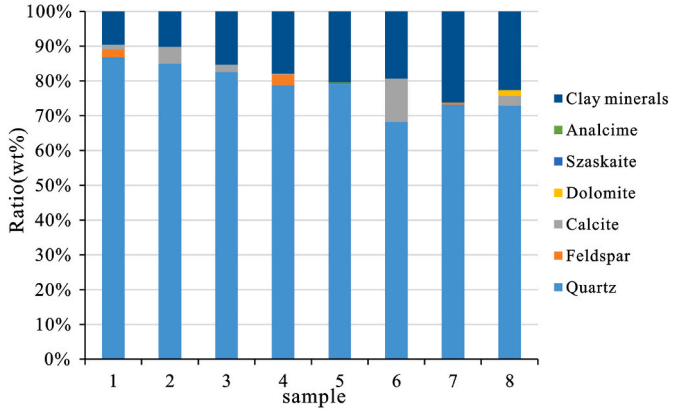

Fig. 5. Mineral compositions and contents of tight gas sandstone samples.

Table 1
The XRD results for bulk and clay mineral testing in samples with distinct lithofacies.

Well	No.	Depth(m)	lithofacies	Porosity(%)	Permeability(mD)	Bulk minerals content(%)						Clay minerals content(%)									
						Quartz(%)	Feldspar(%)	Calcite	Dolomite	Szaskaite	Analcime	Total clay	Illite/Smectite		Kaolinite		Illinite		chlorite	
													Relative	Absolute	Relative	Absolute	Relative	Absolute	Relative	Absolute
J32	1	2941.44	Ps	15.55	0.470	86.7	2.4	1.3				9.6	15.5	1.488	51.0	4.896	17.3	1.661	16.2	1.555
J89	2	3082.32	Ps	14.54	0.401	85.0		4.8				10.2	20.7	2.111	14.3	1.459	30.9	3.152	34.1	3.478
J32	3	2943.07	Sc	9.42	0.362	82.6		2.1				15.3	17.2	2.632	34.8	5.324	18.2	2.785	29.8	4.559
J90	4	2985.98	Cs	9.39	0.316	78.8	3.1	0.2				17.9	18.1	3.240	27.6	4.940	31.7	5.674	22.6	4.045
J7	5	2838.64	Ms	3.52	0.206	79.1				0.2	0.3	20.4	21.7	4.427	28.4	5.794	17.6	3.590	32.3	6.589
J21	6	2875.03	Ms	5.04	0.067	68.3		12.4				19.3	15.7	3.030	32.3	6.234	39.6	7.643	12.4	2.393
J91	7	2979.38	Fs	5.36	0.016	73.2	0.6					26.2	19.4	5.083	34.1	8.943	37.6	9.842	8.9	2.332
J93	8	3037.82	Fs	2.76	0.058	72.9		2.9	1.6			22.6	37.5	8.475	16.8	3.808	23.5	5.322	22.1	4.995

distributions of distinct lithofacies varied dramatically (Figs. 6 and 7). The average porosity of Fs, Ms, Cs, Sc, and Ps lithofacies is 2.9%, 5.9%, 7.3%, 10.5%, and 11.8%, respectively. The average permeability was 0.071 mD, 0.189 mD, 0.551 mD, 0.839 mD and 1.010 mD, respectively. In general, the physical property improves as grain size increases, with pebbly coarse-grained sandstone having the best physical properties and fine-grained sandstone having the poorest. The Sc lithofacies' porosity and permeability have a wide distribution range and a high proportion of medium and low values, primarily as a result of the strong hydrodynamic conditions during Sc lithofacies deposition, the poor sorting of gravel in rocks, the high content of clay minerals in some Sc lithofacies samples, and the close arrangement of particles, which causes low porosity and permeability in some samples. Fig. 7 demonstrates that the permeability of samples with the same porosity differs significantly, which is mainly attributed to the complexity of the microscopic pore structure of tight sandstone reservoirs.

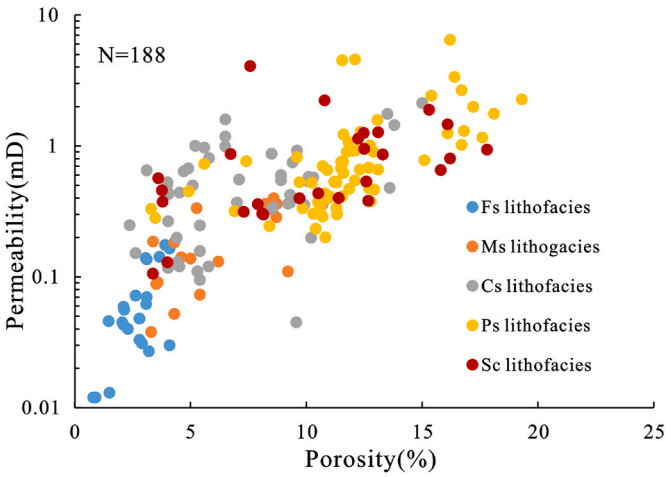

Fig. 7. Cross plot of porosity and permeability of various lithofacies in a tight sandstone reservoir.

4.3. Pore and throat types, geometry

The CTS and SEM observations of the tight sandstone samples of the Lower Shihezi formation reveal six pore types, including residual intergranular pore (R-interGs), intergranular dissolution pore (D-interGs), intragranular dissolution pore (D-intraGs), moldic pore (MP), intercrystalline pore (InterCs) and microfracture (MF), with the average surface porosity of 0.29%, 1.74%, 0.44%, 0.71%, 0.38%, and 0.03%, respectively. R-interGs are irregular angular or polygonal pores retained between grains by the original sediments after a series of diagenesis (Fig. 8b). The primary intergranular pores of sandstone are mostly filled with cement, and only a few R-interGs are preserved, contributing to 8% of the total surface porosity. D-interGs are pores with irregular profiles formed by the dissolution of feldspar, lithic fragments, and soluble components (Fig. 8a–c), which account for 48% of the total surface porosity and are predominantly comprised of feldspar and rock fragments dissolution pores. D-interGs are the main storage space of the Lower Shihezi formation reservoir. D-intraGs are pores with small pore sizes formed by dissolution inside feldspar or debris (Fig. 8e and f), which account for 12% of the total surface porosity. This type of pores contributes very little to the seepage capacity of the reservoir. The MP are those where the feldspar or debris particles are completely dissolved, but the shape of the particles remains (Fig. 8d), accounting for 20% of the total surface porosity. InterCs are developed in clay minerals filled between grains (including chlorite, illite, kaolinite, and illite/smectite mixed layer) (Fig. 8h and i), accounting for 11% of the total surface porosity and contributing little to the physical properties of sandstone. MF includes intragranular fractures (IntraFs) (Fig. 8a, c, d) and intergranular fractures (InterFs) (Fig. 8g), IntraFs are widely distributed in the Lower Shihezi formation sandstones but have little influence on physical properties. InterFs are rarely distributed but can effectively improve pore connectivity and provide channels for fluid migration. The proportions of different pore types in various lithofacies are varied. There are more R-interGs, D-interGs, and MP in Ps, Sc, and Cs lithofacies, whereas there are more D-intraGs and InterCs in Ms and Fs lithofacies, and MF is easily formed in Fs lithofacies.

There are five major throat types of the Lower Shihezi formation sandstone, including pore-shrinking (Fig. 8a), neck-contracted (Fig. 8b), slice-shaped (Fig. 8a), curved sheet (Fig. 8f), and tube bundle throats (Fig. 8i). The grain size of Ps, Sc, and Cs lithofacies is coarser, and there are more pore-shrinking, slice-shaped, and curved sheet throats. Ms and Fs lithofacies have undergone more intense compaction, and there are a lot of clay minerals, so the number of neck-contracted and tube bundle throats is more, and the tube bundle throats of clay minerals have the worst connectivity.

4.4. Pore throat size distribution and connectivity

4.4.1. Pore throat size distribution

The capillary pressure curves of mercury intrusion and extrusion in various lithofacies are depicted in Fig. 9, and their key parameters are listed in Table 2. The capillary pressure curves of various lithofacies differ noticeably. The capillary pressure curves of Ps, Sc, Cs, Ms, and Fs lithofacies gradually become steeper, and the coarser the grain size, the

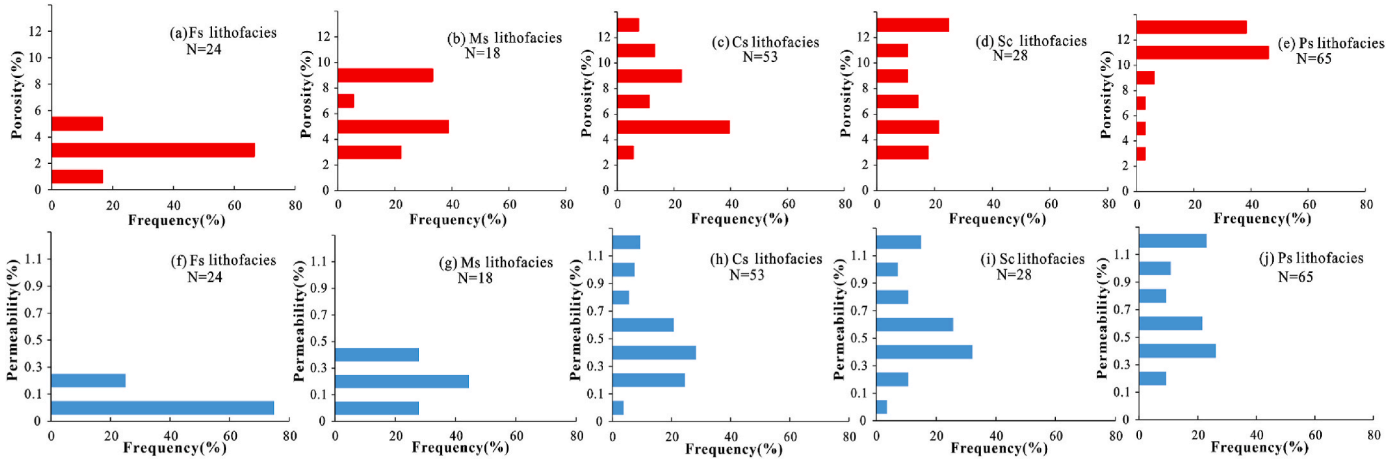

Fig. 6. Distribution of porosity and permeability of different lithofacies in a tight sandstone reservoir.

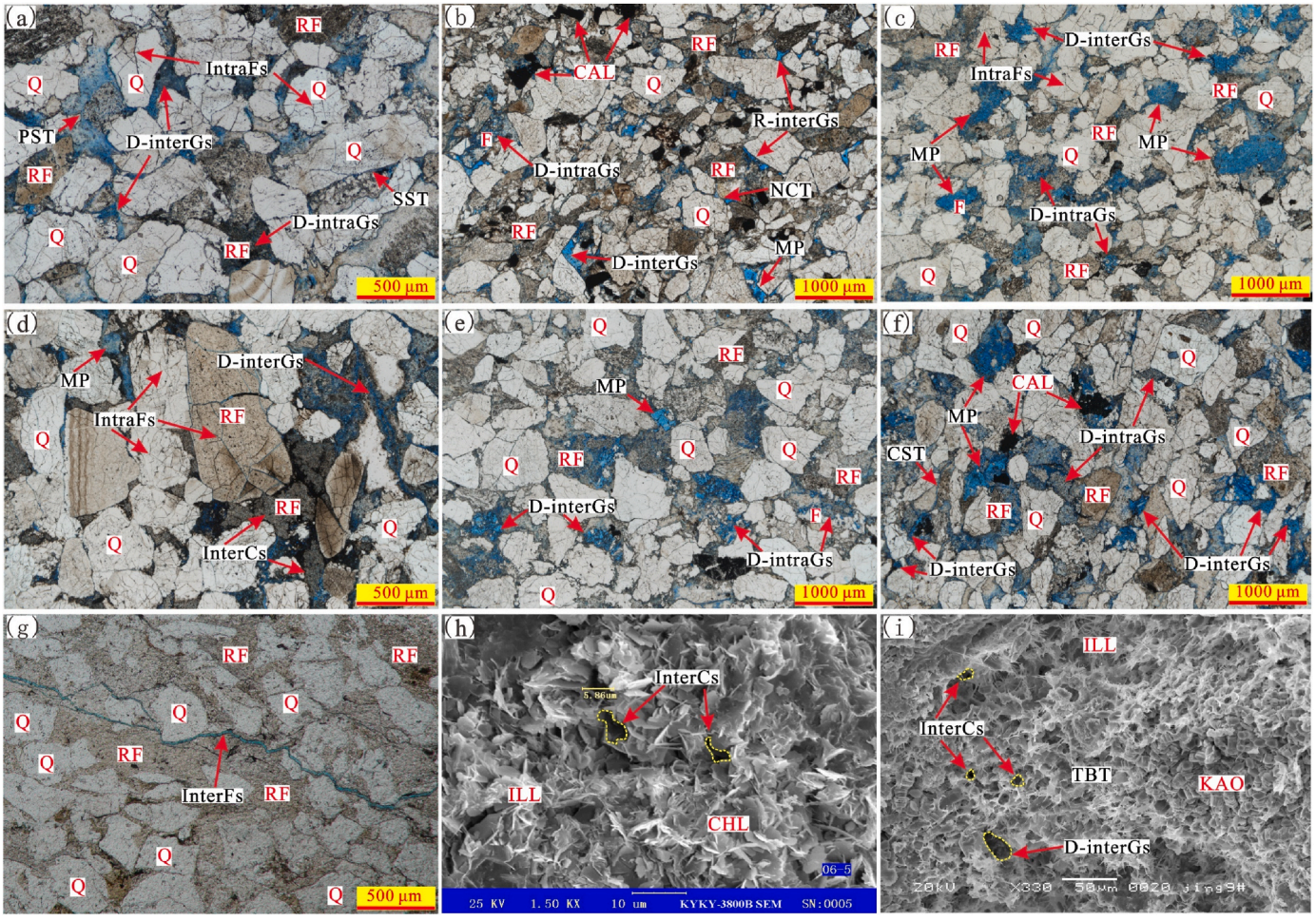

Fig. 8. Photomicrographs showing the lithology, pore, and throat types from CTS and SEM observations. Q: Quartz; F: Feldspar; RF: Rock fragment; CAL: Calcite; KAO: Kaolinite; ILL: Illite; CHL: Chlorite. (a) Pebbly coarse-grained lithic sandstone, well J32, 2941.44 m. (b) Sandy conglomerate lithic sandstone, well J48, 2534.92 m. (c) Coarse-grained lithic sandstone, well J53, 2891.1 m. (d) Pebbly coarse-grained lithic quartz sandstone, well J89, 3081.32 m. (e) Coarse-grained lithic sandstone, well J90, 2969.7 m. (f) Medium-grained lithic quartz sandstone, well J91, 2982.99 m. (g) Fine-grained lithic sandstone, well J69, 2964.77 m. (h) Pebbly coarse-grained lithic quartz sandstone, well J89, 3082.34 m. (i) Fine-grained lithic quartz sandstone, well J9, 2993.79 m. (Note that R-interGs, D-interGs, D-intraGs, MP, InterCs, InterFs, and IntraFs are residual intergranular pores, intergranular dissolution pores, intragranular dissolution pores, mold pores, intercrystalline pores, intergranular fractures, and intragranular fractures, respectively. PST, NCT, SST, CST, and TBT separately refer to pore-shrinking throats, neck-contracted throats, slice-shaped throats, curved sheet throats, and tube bundle throats).

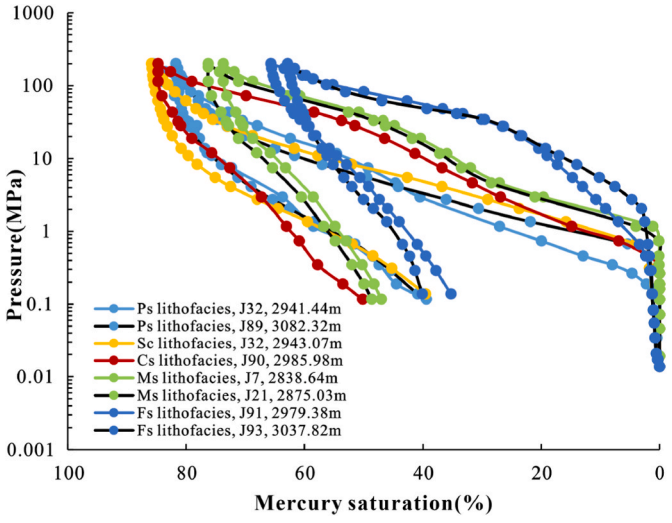

Fig. 9. Capillary pressure curves of mercury intrusion and extrusion in various lithofacies obtained by HPMI.

longer the platform section of the curve (Fig. 9). P_d of Ms and Fs lithofacies are all greater than 0.6 MPa, R_{max} is less than 1 μm, and S_{max} is less than 80%. However, P_d of Ps, Sc, and Cs lithofacies are all less than 0.5 MPa, R_{max} is more than 1.5 μm, and S_{max} is mainly distributed around 85% (Table 2). This indicates that the Ms and Fs lithofacies have more pores and throats with a smaller radius, such as D-intraGs and InterCs, whereas the number of D-interGs and MP in Ps, Sc, and Cs lithofacies is more, with larger pore throat radius and intrusion mercury saturation. The parameters from HPMI in Table 2 also demonstrate the variability of the pore networks of different lithofacies samples. The mean P_d and P_{50} of Ps lithofacies are the smallest, and r_a is the largest.

Fig. 10 depicts pore throat size distribution and its contribution to permeability calculated from HPMI data. It shows that the pore throat size distribution of typical samples of different lithofacies of tight sandstone ranges between 0.004 μm and 2.5 μm, and the pore throat with a radius less than 0.25 μm is distributed in each lithofacies, and the intrusion mercury saturation of pore throat in this range is more than 50%. However, the pore throat radius ranges that mainly contribute to the permeability of typical samples of various lithofacies are notably different. The range of pore throat radius that primarily contributes to permeability in Ps, Sc, Cs, Ms, and Fs samples is 0.25–2.5 μm, 0.16–1 μm, 0.1–1 μm, 0.06–0.63 μm, 0.02–0.25 μm, respectively (Fig. 10). This

Table 2
Mercury intrusion parameters of different lithofacies in tight sandstone reservoirs from HPMI.

Well	No.	Depth(m)	Lithofacies	φ(%)	K(mD)	P_d(Mpa)	P_{50}(Mpa)	r_{max}(μm)	r_{50}(μm)	r_a(μm)	S_{max}(%)	W_e(%)	S_o
J32	1	2941.44	Ps	15.55	0.470	0.220	7.933	3.412	0.095	0.364	85.647	53.972	1.215
J89	2	3082.32	Ps	14.54	0.401	0.457	5.680	1.608	0.129	0.299	81.770	49.969	2.061
J32	3	2943.07	Sc	9.42	0.362	0.463	7.670	1.586	0.096	0.255	85.859	53.930	2.120
J90	4	2985.98	Cs	9.39	0.316	0.491	25.238	1.527	0.030	0.141	84.748	40.806	2.193
J7	5	2838.64	Ms	3.52	0.206	1.102	41.245	0.681	0.018	0.083	73.731	36.204	2.341
J21	6	2875.03	Ms	5.04	0.067	0.940	37.100	0.798	0.020	0.088	76.273	36.204	2.249
J91	7	2979.38	Fs	5.36	0.016	0.660	82.520	0.909	0.009	0.096	65.672	46.295	2.478
J93	8	3037.82	Fs	2.76	0.058	2.044	72.150	0.360	0.010	0.059	62.864	36.203	2.254

Notes: φ-rock porosity; k-rock permeability; P_d-displacement pressure; P_{50}-medium saturation pressure; r_{max}-maximum pore throat radius; r_{50}-median pore throat radius; r_a-average pore throat radius; S_{max}-maximum intrusion mercury saturation; W_e-efficiency of mercury withdrawal; S_o-sorting factor.

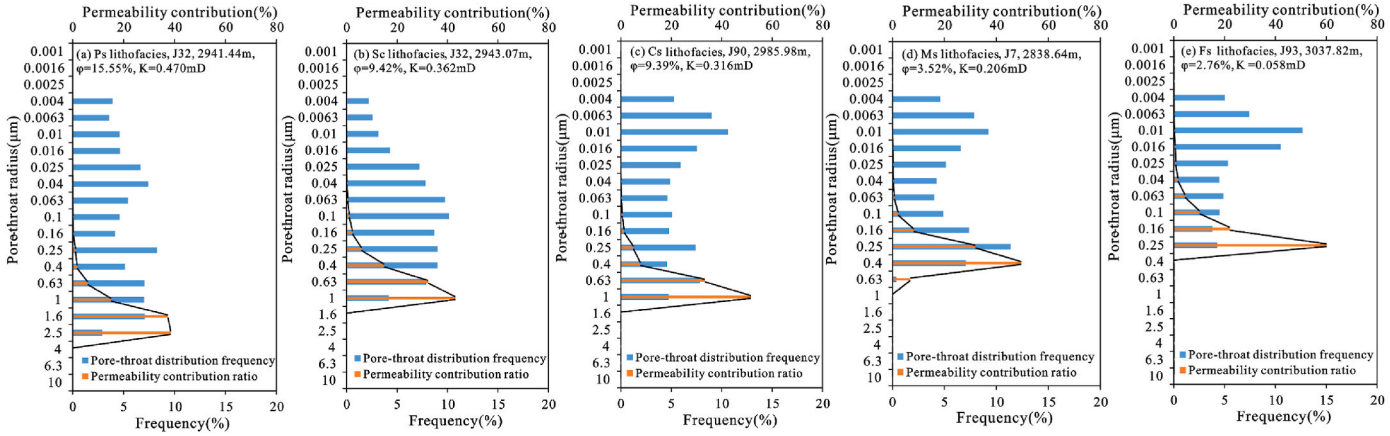

Fig. 10. The pore throat size distribution and its contribution to the permeability of distinct lithofacies obtained by HMPI.

implies that although the pore throat radius range of the lithofacies with the coarser grain size is larger, its seepage capacity is mainly contributed by the larger-radius pore throat. The pore throat radius of the main seepage capacity in Ps lithofacies is the largest, leading to enhanced storage and seepage capacity. In contrast, the pore throat radius of the main seepage capacity in Fs lithofacies is the smallest, resulting in the worst physical properties. It is worth noting that some pore information with larger radii could not be measured due to the pore shielding effect of HPMI.

The T_2 spectrum obtained through the NMR test was converted into pore throat radius (Fig. 11). The pore throat size distribution of the eight

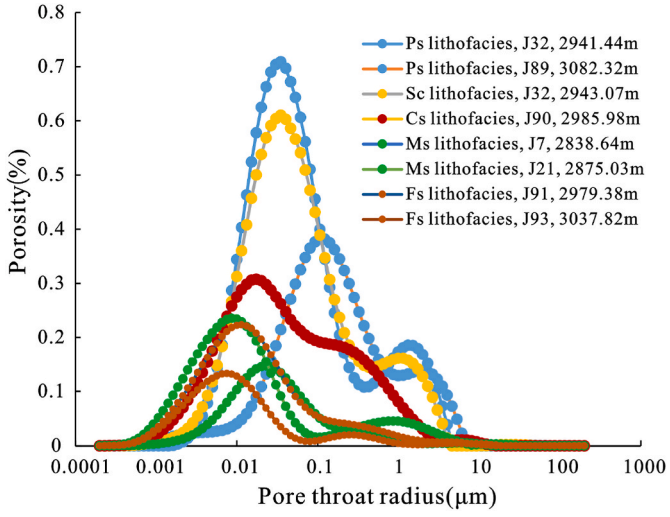

Fig. 11. Pore throat size distribution of different lithofacies obtained by NMR experiment.

samples from different lithofacies exhibits left-skewed bimodal features and the pore throat radius distribution spans between 0.001 μm and 100 μm. The left peak of pore throat size distribution of all samples is primarily dispersed within a range of less than 0.1 μm, while the right peak is distributed in the range of more than 0.1 μm, and the amplitude of the left peak is greater than that of the right peak, implying that tiny pore throats are extensively dispersed throughout each sample of tight sandstone. The pore size distribution of different lithofacies shows significant differences. The radius that corresponds to the left peak of Fs, Ms, Cs, Sc, and Ps increases gradually, and the amplitude of the right peak increases gradually (Fig. 11), indicating that the number of macropores and the contribution of D-interGs and MP to porosity increase with increasing grain size. The right peak porosity segment of the Ps sample is about 0.2%, whereas that of Ms and Fs is less than 0.05%, indicating that the porosity of Ms and Fs lithofacies is primarily contributed by tiny pores, and the number of large pores is extremely low. This is consistent with the previous analysis that there are many D-intraGs and InterCs in Ms and Fs lithofacies. The amplitude difference between the T_2 distribution of saturated water (T_{2s}) and the T_2 distribution after centrifugation (T_{2c}) acquired by NMR can be utilized to evaluate fluid mobility. The movable fluid saturation (S_{mov}) is equal to the ratio of the area between the T_{2s} and T_{2c} spectrum to the area covered by T_{2s}. $T_{2cutoff}$ is the threshold T_2 value for the existence of movable fluid and bound fluid (Zhang et al., 2019; Qiao et al., 2020a). The T_{2s} and T_{2c} spectrum of typical samples from different lithofacies are similar (Fig. 12). The difference in amplitude between the left peak of T_{2s} and T_{2c} is greater than the difference between the right peak of T_{2s} and T_{2c}, suggesting that the small pore throat stores more fluid that can move. In addition, there is a low amplitude at the larger T_2 value in the T_{2c} spectrum, indicating a tiny portion of bound fluid within the larger pores. The main reason bound fluids occur in greater pore radii is that clay minerals adhered to the surface of these pores or throats block the tiny throats that connect the large pores. The range of S_{mov} and movable

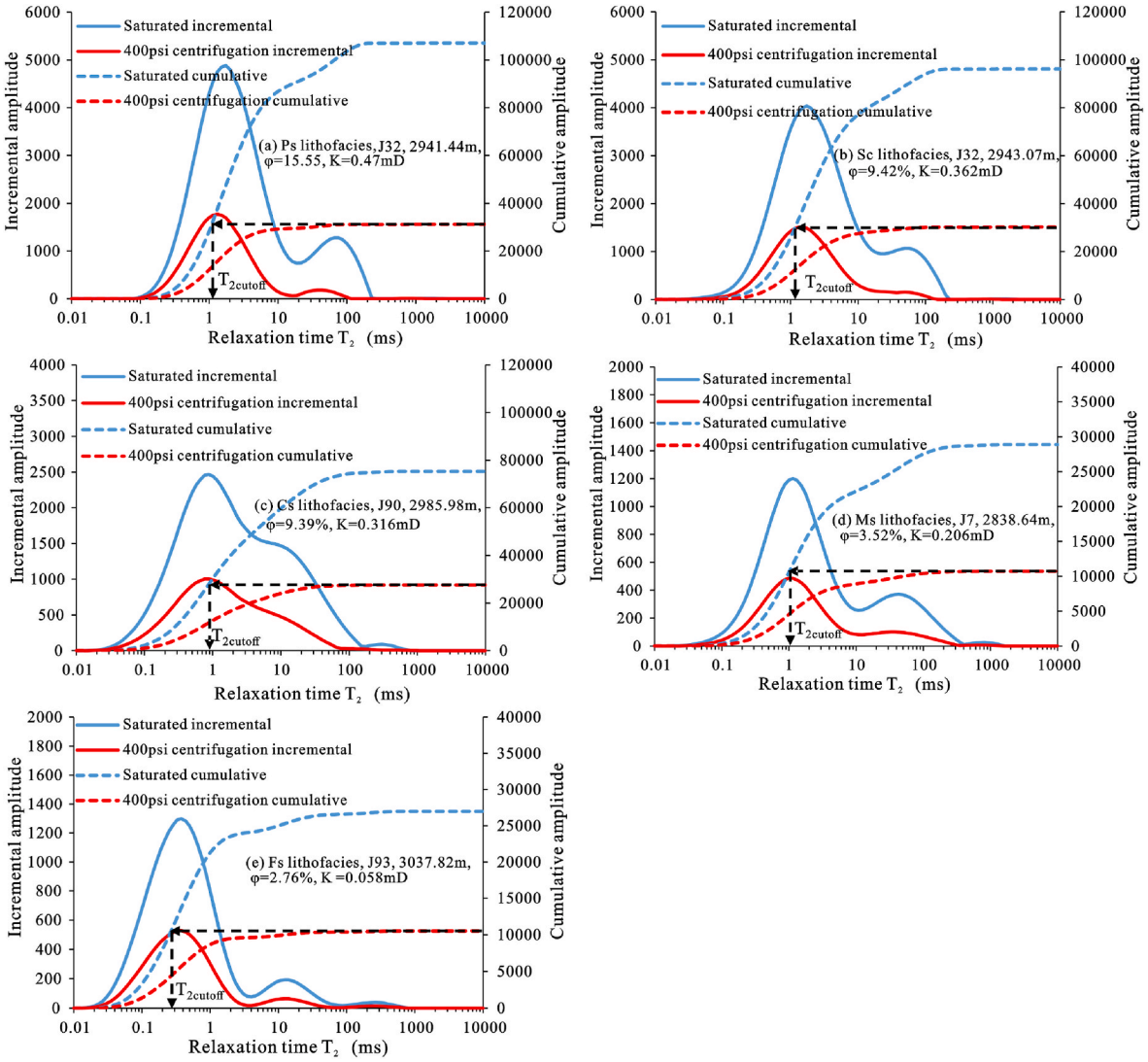

Fig. 12. The range of movable fluids of different lithofacies was evaluated by NMR saturated and centrifuged T_2 spectrums.

fluid porosity (φ_{mov}) is 60.88–72.99% and 1.68–11.02%, respectively (Table 3). The total amplitude difference of the T_{2s} and T_{2c} spectrum of typical samples of Ps, Sc, Cs, Ms, and Fs samples decreases gradually, and the amplitude difference of the right peak becomes significantly smaller, and the saturation of movable fluid decreases in turn (Fig. 12, Table 3), indicating that the larger the particle size of the sample, the greater the number of macropores, the movable fluid is easier to exist in and possesses superior physical properties.

4.4.2. Pore throat connectivity

3D images of the segmented pore system and pore network model of typical samples of different lithofacies obtained by X-CT are shown in Fig. 13, and multiple pore structure parameters derived are listed in Table 4. The segmented pore system represented by color labels can visually characterize the connectivity of the pore network of tight sandstone samples. Pores of the same color labels are interconnected, whereas pores with distinct color labels are isolated or have poor connectivity. (Fig. 13a, b, c, d, e). The pore network model image can

Table 3
Experimental parameters and fractal dimensions of different lithofacies from NMR.

Well	No.	Depth(m)	Lithofacies	NMR experimental parameter					Fractal dimensions of short and long T_2 time					
				$T_{2cutoff}$(ms)	S_{bou}(%)	S_{mov}(%)	φ_{mov}(%)	φ_{bou}(%)	K_s	D_s	R^2	K_l	D_l	R^2
J32	1	2941.44	Ps	1.12	29.10	70.90	11.02	4.53	2.8577	0.1423	0.9098	0.0721	2.9279	0.6250
J89	2	3082.32	Ps	2.86	27.01	72.99	10.61	3.93	2.8682	0.1318	0.8734	0.1073	2.8927	0.6479
J32	3	2943.07	Sc	1.24	31.42	68.58	6.46	2.96	2.4681	0.5319	0.9165	0.0687	2.9313	0.6318
J90	4	2985.98	Cs	0.81	36.68	63.32	5.95	3.44	2.4390	0.5610	0.8796	0.0722	2.9278	0.6707
J7	5	2838.64	Ms	1.07	37.22	62.78	2.21	1.31	2.4933	0.5067	0.9046	0.0648	2.9352	0.7454
J21	6	2875.03	Ms	0.27	35.03	64.97	3.27	1.77	2.3147	0.6853	0.8498	0.0196	2.9804	0.6423
J91	7	2979.38	Fs	0.41	39.12	60.88	3.26	2.10	2.2283	0.7717	0.8505	0.0289	2.9711	0.6566
J93	8	3037.82	Fs	0.31	38.95	61.05	1.68	1.08	2.0114	0.9886	0.8491	0.0186	2.9814	0.7412

Notes: $T_{2cutoff}$-the cutoff value of T_2 distribution, S_{bou}-bound fluid saturation, S_{mov}-movable fluid saturation, φ_{mov}-movable fluid porosity, φ_{bou}-bound fluid porosity, D_s-fractal dimensions of the small pore, D_l-fractal dimensions of the large pore, R^2-correlation coefficient, K-the slope of the fractal curve.

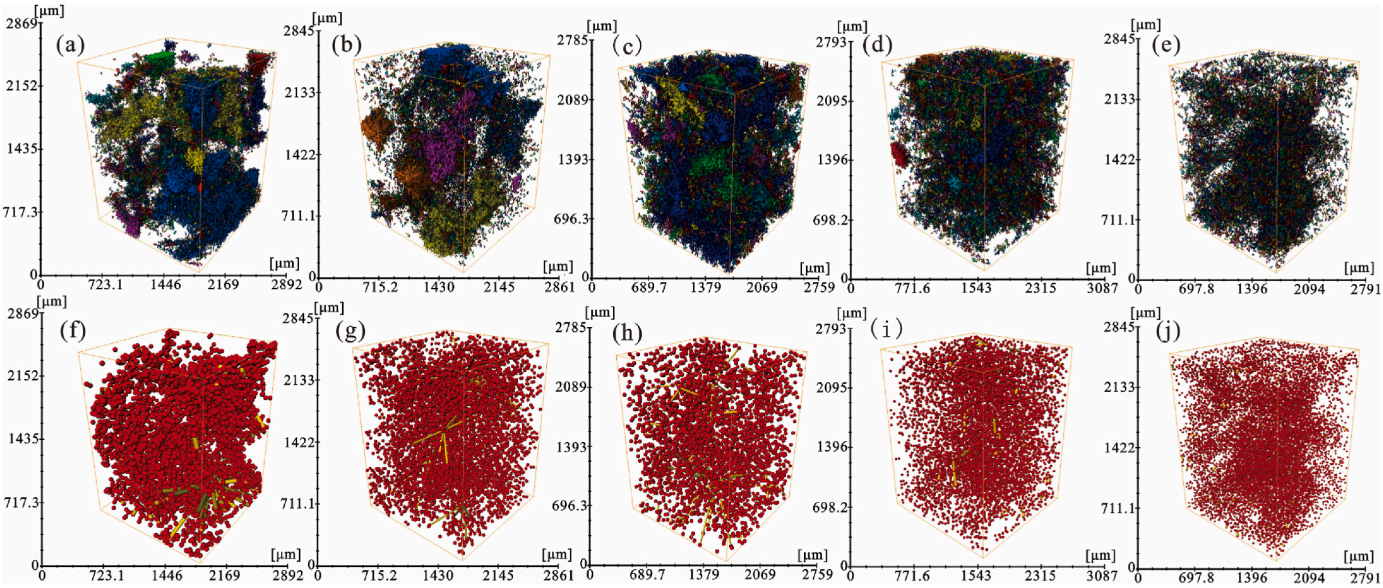

Fig. 13. The 3D images of separated pore systems and pore network modeling (PNM) of various lithofacies from Micro-CT scanning (Pores of the same color in the adjacent area of the separated pore systems represent connected pores. The red balls and yellow sticks in PNM represent pores and throats of distinct sizes obtained using the maximum spherical algorithm, respectively). (a), (b), (c), (d), and (e) are the separated pore systems of typical samples of Ps lithofacies (J32, 2941.44 m), Sc lithofacies (J32, 2943.07 m), Cs lithofacies (J90, 2985.98 m), Ms lithofacies (J7, 2838.64 m) and Fs lithofacies (J93, 3037.82 m), respectively. (f), (g), (h), (i), and (j) are the PNM of typical samples of Ps lithofacies (J32, 2941.44 m), Sc lithofacies (J32, 2943.07 m), Cs lithofacies (J90, 2985.98 m), Ms lithofacies (J7, 2838.64 m) and Fs lithofacies (J93, 3037.82 m), respectively. (For interpretation of the references to color in this figure legend, the reader is referred to the Web version of this article.)

Table 4
Pore structure parameters of different lithofacies based on the X-CT test.

Well	No.	Depth (m)	Lithofacies	Average pore volume/μm^3	Average pore surface area/μm^2	Average coordination number	Average pore radius/μm	Average throat surface area/ μm^2	Average throat radius/ μm	Average throat length/μm
J32	1	2941.44	Ps	50700.21	22,854.03	1.45	15.23	173.42	3.38	386.13
J32	3	2943.07	Sc	20,345.7	7615.87	1.25	13.33	95.06	2.71	224.89
J90	4	2985.98	Cs	20,272	8957.74	1.24	10.44	35.91	2.64	184.38
J7	5	2838.64	Ms	17,022.2	8001.89	1.04	9.92	25.76	2.13	91.4
J93	8	3037.82	Fs	5163.75	2593.57	1.03	9.2	13.15	1.78	50.17

directly observe the size and configuration relationship of pores and throats. The red spheres and yellow cylinders in this image represent pores and throats of different sizes, respectively (Fig. 13 f, g, h, i, j). Typical samples of different lithofacies of tight sandstone in the research area have noticeable variances in pore throat size and spatial assemblages (Fig. 13, Table 4). The volume of pore space covered by each single color label in typical samples of Ps, Sc, and Cs lithofacies is large. However, multiple color labels in Ms and Fs lithofacies images appear interactively, and the pore space volume covered by the single color label is small, which indicates Cs lithofacies have better pore throat connectivity. The average coordination number of typical samples of Ps, Sc, Cs, Ms, and Fs lithofacies is 1.45, 1.25, 1.24, 1.04, and 1.03, respectively, and the average throat radius and length decrease successively (Table 4), implying that the pore throat connectivity degrades with the decrease of sample grain size. The red spheres and yellow cylinders in the pore network model of the Ms and Fs sample have smaller volumes and fewer yellow cylinders (Fig. 13i and j), with poor pore throat connectivity, which is consistent with the CTS and SEM findings that there are more D-intraGs, InterCs and tube bundle throats in Ms and Fs lithofacies. Ps, Sc, and Cs lithofacies contain more composite pores composed of D-interGs, MP, and R-interGs, so the volume of red spheres and yellow cylinders in the pore network model image is larger, and there are more yellow cylinders connected by single red spheres (Fig. 13 f, g, h), with good pore throat connectivity. The Ps lithofacies have the largest pore throat radius and the best connectivity.

4.5. Fractal characteristics

NMR experiments can identify pores at all scales without damaging samples (Zhang et al., 2019; Guo et al., 2019; Wu et al., 2019; Qiao et al., 2020a). Hence, based on NMR data, the fractal characteristics of the pore structure of sandstone samples from the Lower Shihezi Formation were analyzed in detail. The relationship between $\lg(S_v)$ and $\lg(T_2)$ of representative samples of different lithofacies is shown in Fig. 14. The fractal curve is divisible into two parts, and the fractal inflection point is $T_{2cutoff}$, implying that the pores of tight sandstone reservoirs have bi-fractal characteristics. The orange curve on the right corresponds to a larger T_2 value and represents large pores, such as D-interGs, MP, and R-interGs, which typically store movable fluids. The blue curve on the left corresponds to a shorter T_2 time, representing tiny pores, such as D-intraGs and InterCs, whose stored fluid is bound and cannot be produced. By fitting the slopes of the two lines on the left and the right, respectively, the fractal dimension D_s of the small pore and D_l of the large pore can be derived (Fig. 14, Table 3). Generally, pore heterogeneity enhances with the increase of fractal dimension (Li, 2010; Qu et al., 2020). The range of D_s is 0.1318–0.9886, which does not fall within the theoretical range of pore fractal dimension ($2 \leq D < 3$) (Zheng and Yu, 2012), but the value of D_s can still be used to evaluate the pore heterogeneity (Li, 2010). The range of D_l is 2.8927–2.9814, with an average of 2.9435, indicating that macropores follow the fractal principle, and all samples have strong heterogeneity of macropores. The

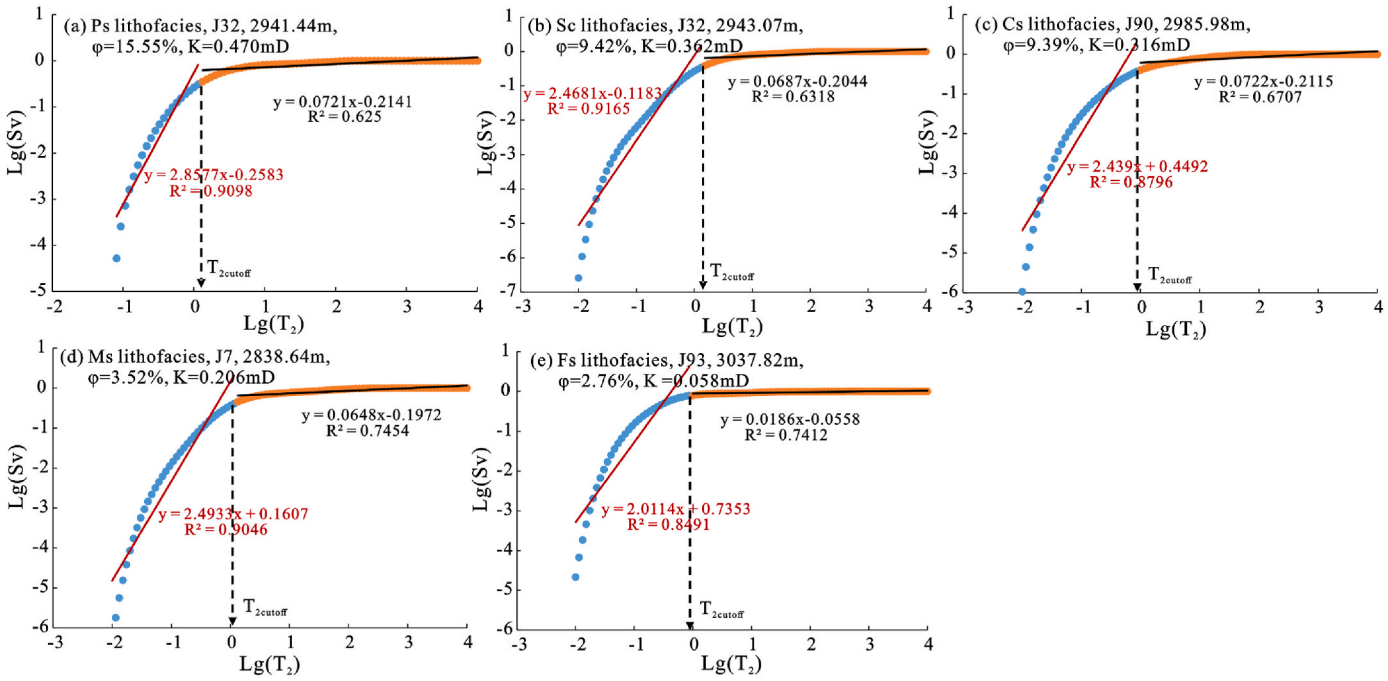

Fig. 14. Fractal curves of typical samples of different lithofacies calculated based on NMR T_2.

average D_s and D_l of Ps, Sc, Cs, Ms, and Fs lithofacies grow gradually (Table 3), implying that the pore heterogeneity of Fs lithofacies dominated by the left-skewed bimodal T_2 distribution is the strongest. In addition, D_l is greater than D_s in all samples, as the morphology and size heterogeneity of D-interGs and R-interGs corresponding to long T_2 time is more pronounced than that of D-intraGs and InterCs corresponding to short T_2 time.

5. Discussion

5.1. Correlation between fractal dimension, physical properties, and microstructural parameters

Physical properties correlate with the fractal dimension of pores in tight sandstone reservoirs (Katz and Thompson, 1985; Broseta et al., 2001; Guo et al., 2019; Zhu et al., 2018; Nie et al., 2021). Both porosity and permeability decrease as fractal dimension D_s and D_l grow, and the corresponding correlation coefficients are 0.7885, 0.6074, 0.6481, and 0.7708, respectively (Fig. 15). The correlation coefficient between

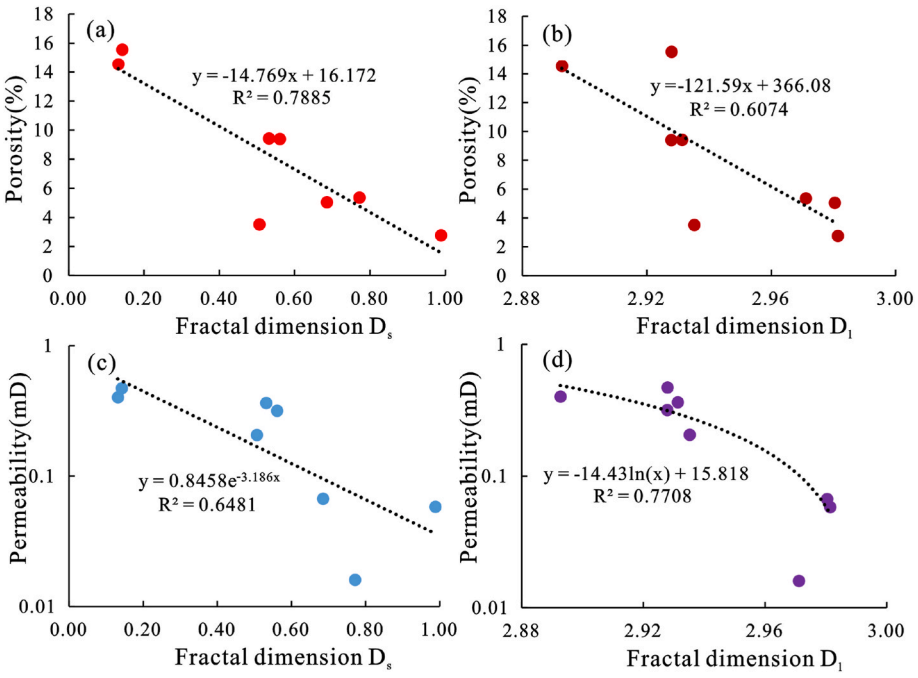

Fig. 15. The correlations between porosity, permeability, and fractal dimensions from NMR-derived.

porosity and D_s is higher than that between porosity and D_l (Fig. 15a and b), showing that the porosity tends to decrease as the pore heterogeneity intensifies. This is primarily because of the more significant the pore heterogeneity, the larger the pore specific surface area, and the smaller the contribution to porosity. The correlation coefficient between permeability and D_l is higher than that between it and D_s (Fig. 15c and d), suggesting that the decrease in permeability is more noticeable as the variability of large pores increases, that is to say, the larger the contribution of large pores to permeability, which is consistent with the previous understanding that permeability of tight sandstone samples is primarily contributed by large pores based on HPMI results analysis (Fig. 10). The D_l of pebbly coarse-grained sandstone sample No. 1 is 2.9279 (Table 3), with a small fractal dimension, contains more D-interGs and R-interGs (Fig. 8a). The average pore radius is large, and the pore size and morphology are more homogeneous, so it has higher porosity and permeability.

The relationship between fractal dimension and P_d, P_{50}, r_a, and S_{max} derived by HPMI is depicted in Fig. 16. The fractal dimensions D_s and D_l are positively correlated with P_d and P_{50}, showing that pore heterogeneity increases with the rise of P_d and P_{50}. The fractal dimensions D_s and D_l are negatively correlated with r_a and S_{max}, indicating that the size and morphology of pores become more homogeneous with the increase of r_a and S_{max}. Furthermore, the correlation coefficients between fractal dimensions D_s and P_d, P_{50}, r_a, and S_{max} are greater than those between dimensions D_l and P_d, P_{50}, r_a, and S_{max}. This is because HPMI mostly measures pores less than 1 μm, which mainly reflects the distribution characteristics of pore throats with smaller radii.

The fractal dimension was negatively correlated with the average pore volume, average pore radius, average throat radius, and average coordination number obtained by X-CT (Fig. 16e-h). The correlation coefficients of fractal dimensions.

D_s and D_l with the average throat radius are larger than their correlation coefficients with the average pore radius (Fig. 16f and g), which indicates that with the increase in throat radius, the number of tiny throats connecting large pores decreases, and the fractal dimension is easier to decrease. The size and morphology of pore throats in tight sandstone samples are more homogeneous, and the physical properties are better. For example, the average throat radius of pebbled coarse-grained sandstone sample No.1 is greater than that of sandy conglomerate sample No.3, and the fractal dimension is smaller (Table 3, Table 4).

5.2. *The controlling effect of diagenesis on pore structure heterogeneity*

The pore types of the Lower Shihezi formation are predominately secondary dissolved pores, the proportion of primary pores is minimal, and the complexity of pore size and distribution is high, indicating that diagenesis is the main cause governing the heterogeneity of pore structure. A detailed analysis of the effects of diagenesis type and intensity on the variability of pore structure is helpful to the prediction of high-quality tight sandstone gas reservoirs.

5.2.1. *Compaction*

Compaction can directly alter the pore structure characteristics of sandstone, which is a significant contributor to the loss of original porosity in tight sandstone reservoirs (Cook et al., 2011; Higgs et al., 2007; Wang et al., 2020c; Zhang et al., 2022). The intensity of compaction is usually influenced by the mineral composition, burial depth, temperature, and stress conditions of reservoirs (Schmoker and Gautier, 1988; Pittman and Larese, 1991; Fawad et al., 2011). The

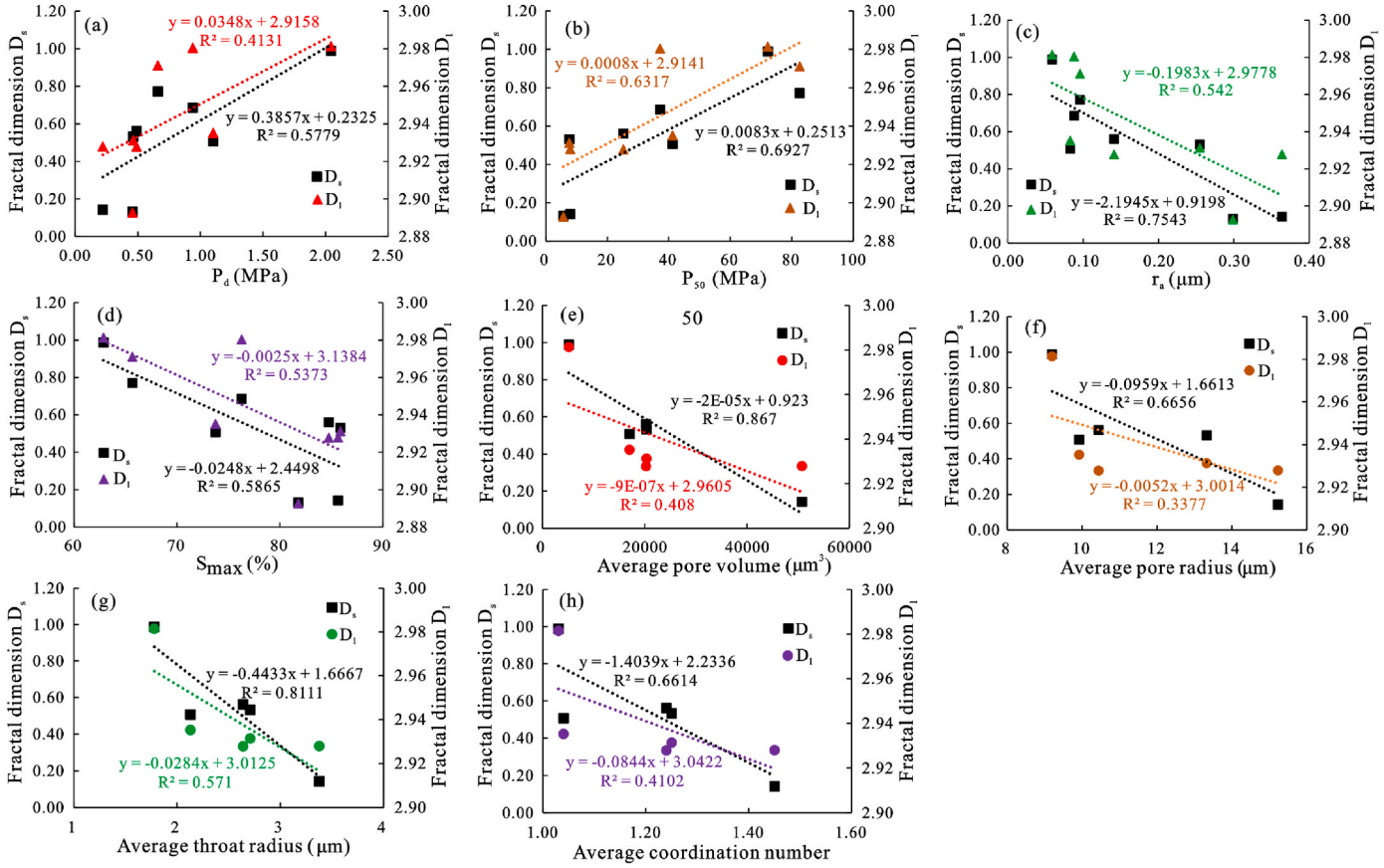

Fig. 16. The correlations between fractal dimensions and microstructure parameters (a, b, c, and d are displacement pressure, medium saturation pressure, average pore throat radius, and maximum intrusion mercury saturation from HPMI, respectively; e, f, g, and h are average pore volume, average pore radius, average throat radius and average coordination number from X-CT, respectively).

buried depth of the target layer in the study region is more than 3000 m, which is a deeply buried reservoir. Mica and plastic debris particles exhibit extreme deformation (Fig. 8b). The contact mode of debris particles is point-line or concave-convex contact, and there are many IntraFs in quartz particles (Fig. 8 a-g), which shows that strong compaction causes the breakage of rigid particles and the distortion of plastic particles. Cross plots of intergranular pore volume (IGV) and cement content can be used to quantify porosity loss due to cementation and compaction (Fig. 17). In the majority of samples, the porosity reduction owing to compaction is higher than 50%, and it is greater than the porosity reduction owing to cementation. It is further indicated that strong compaction is the key factor in the loss of original porosity and the narrowing of the pore throat in the Lower Shihezi formation sandstone.

Although compaction resulted in a significant reduction of primary pores, the porosity reduction rates of different samples showed certain differences (Fig. 17). Primary intergranular pore volume and quartz content exhibit a strong correlation (Fig. 18a). The volume of retained primary intergranular pore increases as the quartz content increases, indicating that quartz resists compaction to a certain extent. In addition, the r_a and S_{max} improve with increasing quartz content (Fig. 18b and c), whereas the fractal dimension decreases (Fig. 18d). This is because quartz not only resists compaction, but also the intragranular fractures formed by quartz fracture can improve physical properties, and samples with high quartz content retain more primary pores, which can provide migration channels for diagenetic fluids, hence promoting dissolution. As a result, a pore network composed of R-interGs, D-interGs, and MP is formed, and the pore structure becomes more homogeneous.

5.2.2. Cementation

5.2.2.1. Calcite cements. Calcite is an important type of carbonate cement in the reservoirs of the Lower Shihezi formation, including calcite formed in the eogenetic stage and ferrocalcite formed in the mesogenetic stage, among which the content of the eogenetic calcite is the most abundant. Calcite is orange under cathodoluminescence (CL) conditions (Fig. 19a), and the eogenetic calcite fills the primary pores (Fig. 19d), blocking the pores and throats, resulting in poor reservoir physical properties. However, early diagenetic calcite can also provide the material basis for dissolution and form dissolution pores. Compaction of the adjacent mudstone can expel alkaline fluids rich in Ca^{2+} and facilitate calcite cementation (El-ghali et al., 2006; Dutton, 2008; Taylor and Machent, 2011; Gao et al., 2022; Yang et al., 2022). These cements can effectively inhibit compaction to a certain extent, keep the rock particles in point-line contact, and preserve the original porosity in the middle of some sand bodies. During the middle diagenetic period, some igneous debris dissolution provided abundant Fe^{2+}, and the early calcite cement and some debris dissolution generated abundant Ca^{2+}, thus forming ferrocalcite (Fig. 19b), which was difficult to dissolve in an acidic fluid environment, resulting in extremely destructive to the pore structure. Average pore throat radius, fractal dimension, and porosity all have a weakly negative correlation with calcite content (Fig. 20a, b, c), a moderate to weak negative correlation between calcite content and permeability (Fig. 20d), and the correlation coefficient between calcite content and permeability is significantly greater than that between calcite content and porosity. This suggests that calcite generally has a negative influence on pore structure. The average pore throat radius decreases, connectivity worsens, and heterogeneity is enhanced as the calcite content increases. Moreover, Fig. 19a, b, and d indicate that calcite filling pore space is easy to block the throat, resulting in some pores becoming isolated pores, while throat radius and pore throat connectivity are the key factors determining the permeability of rock samples. Therefore, with the increase of calcite content, the decrease in permeability is more evident than that of porosity and pore throat radius.

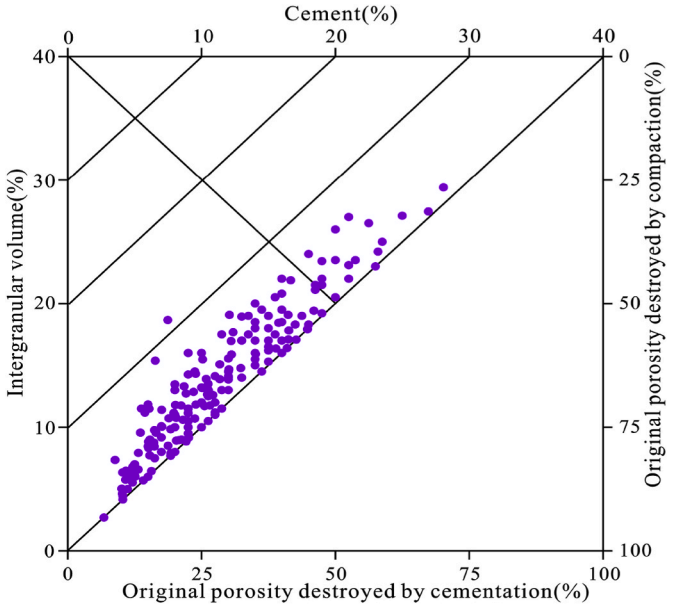

Fig. 17. The plot of the impacts of compaction and cementation on the porosity losses of the Lower Shihezi formation tight sandstone samples (diagram after Ehrenberg, 1989).

5.2.2.2. Clay minerals cements. Previous research has revealed that the effect of clay minerals on pore structure is quite complex, and different types and contents of clay minerals have diverse impacts on pore structure (Spencer, 1989; Higgs et al., 2007; Liu et al., 2018; Mahmic et al., 2018). Grain-coating chlorite content within a certain range can inhibit compaction and play a positive role in the pore structure. Filling pores with large amounts of clay minerals reduces pore space and blocks throats, thereby damaging reservoir porosity and permeability (Bjørlykke, 2014; Qiao et al., 2020b; Wang et al., 2020c). The clay minerals of the target layer are mainly kaolinite and illite. The principal source of kaolinite is the recrystallization of SiO_2 and Al^{3+} formed by feldspar dissolution under the action of the acidic fluid (Dixon et al., 1989; Wilkinson et al., 1997; Worden and Morad, 2003). The CTS image clearly shows that the secondary dissolution pores created by feldspar dissolution are filled with kaolinite (Fig. 19c). Kaolinite glows indigo blue under CL (Fig. 19a), and SEM images show that kaolinite is a booklet or worm-shaped filling pores or dispersed on particle surfaces (Fig. 19e and f). The content of feldspar in the target layer reservoir is very low, because it is a coal-bearing formation, and a considerable number of organic acids generated in the beneath source rocks during hydrocarbon generation are conducive to the dissolution of feldspar, thus forming a large amount of kaolinite. Illite and illite/smectite mixed layers are filamentous or scaly (Fig. 19g and h), and are predominantly dispersed on the surface of dissolved particles. When the potassium ions generated by the complete dissolution of potash feldspar cannot be efficiently transported and discharged, the feldspar dissolution products tend to form illite (Meadows and Beach, 1993; Yu et al., 2019). The distribution of rose-shaped (Fig. 19h) or lining-shaped (Fig. 19i) chlorite on the surface of particles or in the pores has a damaging effect on the pore structure.

A significantly adverse association exists between total clay mineral content and pore throat parameters (Fig. 21 a, b, e, f, g), demonstrating that as total clay mineral content increases, the average pore throat radius, pore space volume, and S_{mov} decrease dramatically. This is because the reservoirs of the Lower Shihezi formation are braided river deposits with near provenance, clay minerals are the primary component of cement, and the average total clay mineral content of eight tight sandstone samples is 17.7% (Table 1). The contribution of InterCs to the

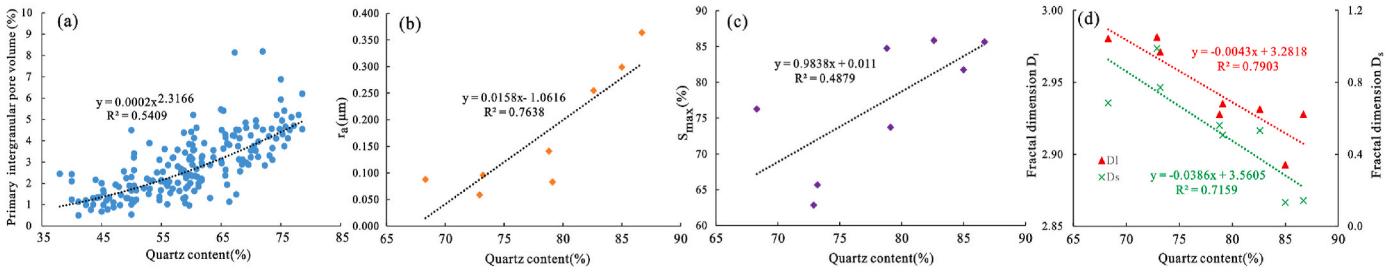

Fig. 18. The relationships between quartz content and microstructure parameters (a, primary intergranular pore volume from CTS; b, average pore throat radius from HPMI; c, maximum mercury saturation; d, fractal dimension D_s and D_l from NMR).

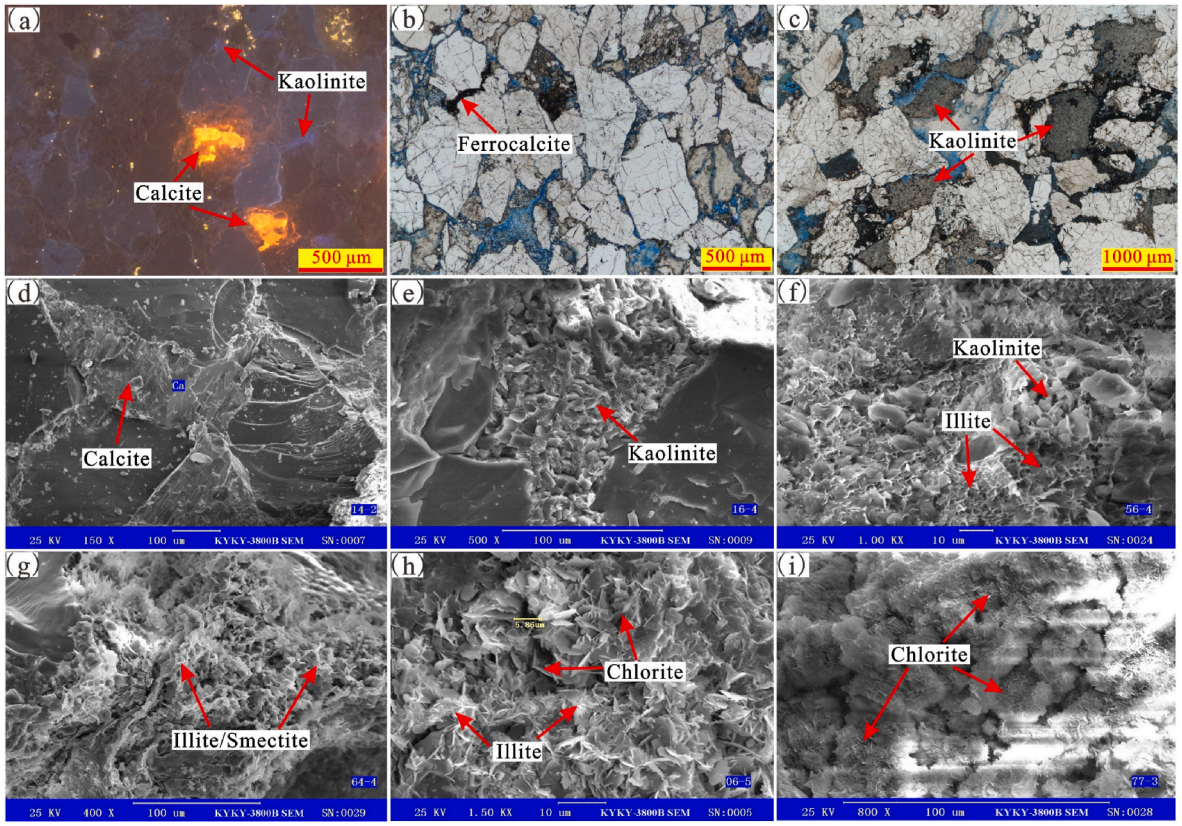

Fig. 19. The photomicrographs of calcite and clay minerals cementation characteristics in tight sandstone gas reservoirs. (a) Cs lithofacies, well J91, 2996.06 m; (b) Cs lithofacies, well J90, 2985.98 m; (c) Sc lithofacies, well J89, 3081.32 m; (d) Ms lithofacies, well J21, 2875.03 m; (e) Ms lithofacies, well J92, 3031.72 m; (f) Ms lithofacies, well J92, 3073.88 m; (g) Fs lithofacies, well J93, 3037.82 m; (h) Ps lithofacies, well J89, 3082.34 m; (i) Ms lithofacies, well J7, 2838.64 m.

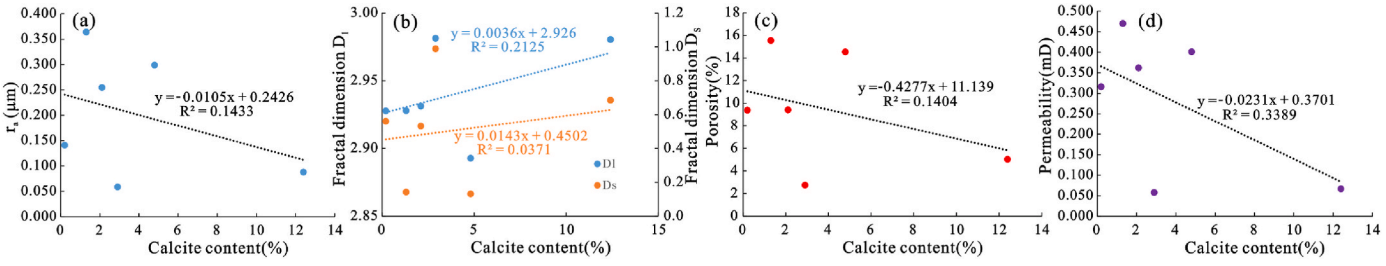

Fig. 20. Plots showing the effects of calcite content on pore structure parameters (a, average pore throat radius from HPMI; b, fractal dimension D_s and D_l from NMR) and physical properties (c, porosity; d, permeability).

pore space is very small, and a large amount of clay mineral cement fills the primary pores and secondary dissolution pores, causing smaller pore throat radius and poor connectivity, and some pores and throats are entirely blocked. The correlation coefficient of the total clay mineral content with the D_s is higher than that with the D_l (Fig. 21c and d), which shows that the heterogeneity of pores is more likely to become stronger as the total content of clay minerals rises. Because of the small pore radius of InterCs or D-intraGs, when more clay minerals interlace

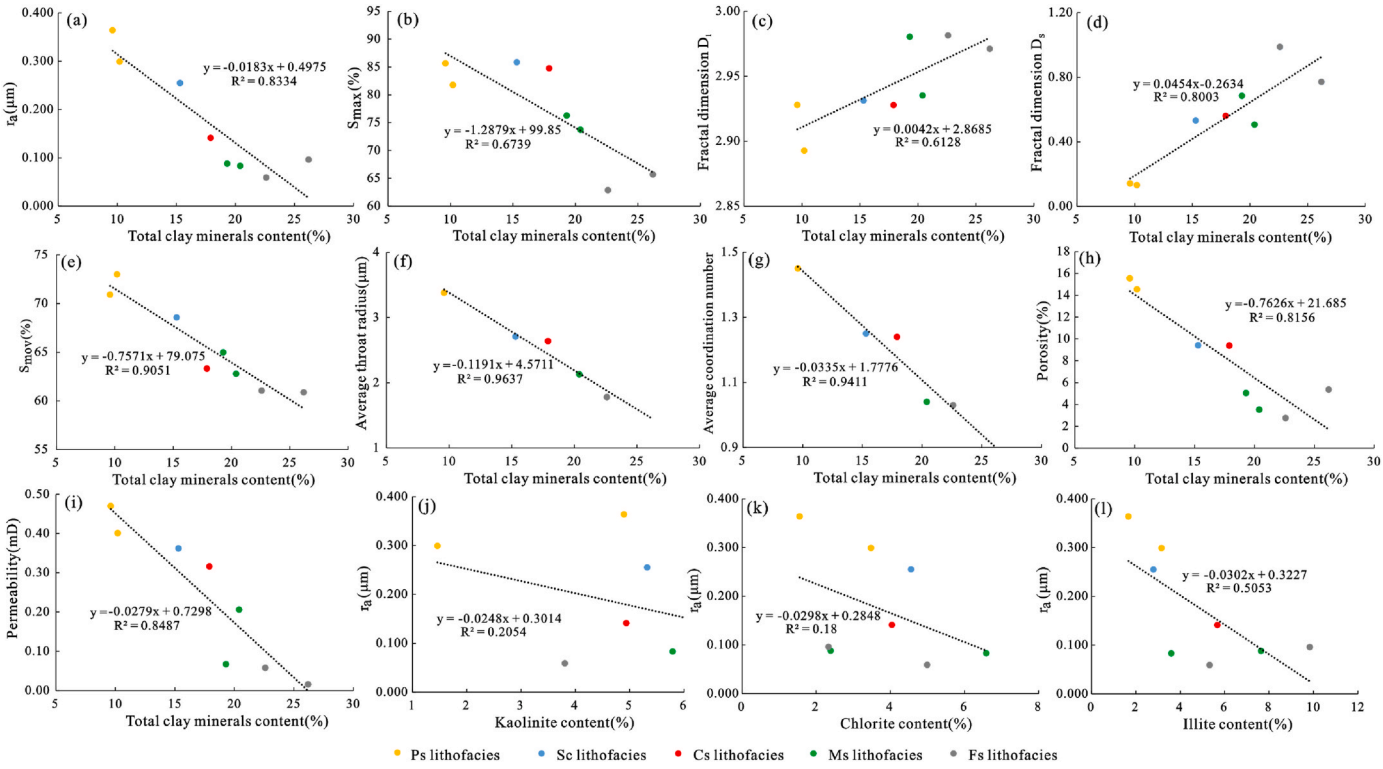

Fig. 21. Plots of the effects of total clay minerals content on microstructure parameters (a and b are the average pore throat radius and maximum mercury saturation respectively from HPMI; c, d, and e are the fractal dimension of the large pore, the small pore, and the movable fluid saturation from NMR, respectively; f and g are the average throat radius and average coordination number respectively from X-CT) and physical properties (h, porosity; i, permeability) in different lithofacies; Plots of the effects of single clay mineral content (j, kaolinite; k, chlorite; l, illite) on average pore throat radius from HPMI in different lithofacies.

and distribute in these pores, the shape and distribution of the pore are more complex, and the effective micropore pore space shrinks. Clay minerals are highly damaging to pore structure, which leads to a decline in reservoir physical properties (Fig. 21 h, i). Moreover, as the particle size becomes finer, the overall clay mineral content increases, and the physical property degrades. Fs and Ms lithofacies have the smallest average pore throat radius and the worst physical property. The cross plots of kaolinite, chlorite, illite and average pore throat radius (Fig. 21j, k, l) show that illite has the best negative correlation with average pore throat radius, indicating that filamentous illite has the most destructive effect on pore throat size and connectivity. The effect of clay minerals on pore structure also depends on the type of clay minerals.

5.2.3. Dissolution

The dissolved pores are the primary storage and seepage space of the Lower Shihezi formation. According to CTS results, the average surface porosity of secondary dissolution pores is 1.74%, contributing to 80% of the total surface porosity. The dissolution of unstable components in the clastic particles of tight sandstone results in a large number of D-interGs and D-intraGs (Fig. 8 a, b, c). When the particles are completely dissolved by strong dissolution, MP can be formed (Fig. 8c). D-interGs and MP account for 68% of the total surface porosity. These unstable components (such as feldspar and debris) provide an abundant material base for dissolution. Previous studies have found that dissolution requires adequate fluid-rock interaction and efficient fluid transport pathways (Barth and Bjørlykke, 1993; Schmid et al., 2004; Zheng and Ying, 1997; Li et al., 2016, 2021; Zhang et al., 2018; Fan et al., 2019). The coal seams and dark mudstones of the Shanxi and Taiyuan formations, adjacent to the reservoirs of the Lower Shihezi formation, are high-quality source rocks. A large number of organic acids generated by the thermal evolution of organic materials can migrate to the sandstone reservoirs of the Lower Shihezi formation through fractures, unconformity surfaces, and pore systems, providing abundant acidic fluids. The dissolution intensity was effectively increased (Surdam et al., 1989; Bai et al., 2020; Li et al., 2020b). The extremely low content of feldspar and a large amount of authigenic kaolinite in the reservoir also indicates that the reservoir has experienced strong dissolution. The pore network composed of R-interGs in the sandstone reservoir of the Lower Shihezi formation provides a pathway for the interaction between acidic fluid and unstable clastic particles and enables the dissolution products to be transported away from the dissolution site, forming composite pores composed of R-interGs and dissolution pores (Fig. 8b), thereby expanding the reservoir pore space.

The highly positive correlation between dissolution surface porosity and average pore throat radius (Fig. 22a), movable fluid saturation (Fig. 22b), and reservoir physical properties (Fig. 22c and d) indicates that dissolution has a significant effect on reservoir pore space and physical properties. With the increase of dissolution surface porosity, the average pore throat radius increases, porosity increases significantly, the effective pore space for fluid seepage increases, and permeability improves dramatically. The dissolution surface porosity of various lithofacies shows a noticeable difference (Fig. 22). The coarser the lithofacies, the greater the dissolution surface porosity, which is due to a large number of R-interGs in the coarser lithofacies, which is conducive to the migration of acidic fluid, and thus the formation of more composite pores composed of R-interGs and dissolution pores, such as pebbly coarse-grained sandstone samples (Fig. 8a). However, after compaction and cementation, the samples with fine grain size almost have no primary pores, and the acidic fluid cannot fully interact with the rock particles and migrate effectively, thus forming more D-intraGs. Moreover, the dissolution products cannot be effectively discharged, and the cement is formed at the edges of the dissolution particles, such as in the fine-grained sandstone samples (Fig. 8a; Fig. 19g). The isolated and poorly connected D-intraGs almost do not contribute to the reservoir's effective storage space and seepage capacity, whereas D-interGs and MP effectively increase the pore throat radius and improve the connectivity,

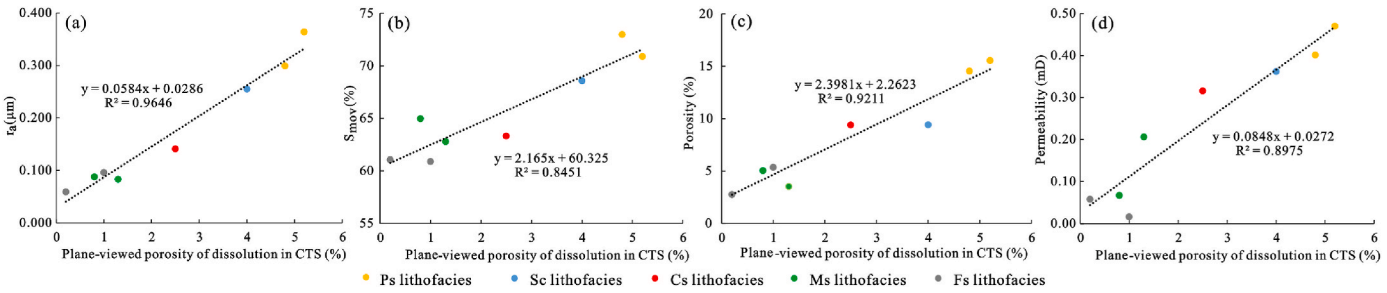

Fig. 22. Plots showing the influences of plane-viewed porosity of dissolution in CTS on microstructure parameters (a, the average pore throat radius from HPMI; b, movable fluid saturation from NMR) and physical properties (c, porosity; d, permeability) in samples with different lithofacies.

thereby significantly increasing the reservoir's porosity and permeability.

5.3. Implications for high-quality reservoir prediction of tight sandstone

The sand bodies of the Lower Shihezi formation are widely distributed in the study area, and the high-quality reservoirs with relatively high porosity and high permeability are less distributed and difficult to predict, while the high-quality reservoirs are the focus of tight sandstone gas development (Taylor et al., 2010; Yu et al., 2019). The diagenesis of tight sandstone samples with diverse lithofacies of the Lower Shihezi formation is highly complex, resulting in differences in pore structure and physical properties. High-quality reservoirs are primarily distributed in Ps and Sc lithofacies with high quartz content, which have undergone relatively weak compaction, strong dissolution, and weak cementation (Fig. 23). They have a large proportion of R-interGs, D-interGs, MP, and movable fluid, which makes it simple to form a homogeneous pore network with a large pore radius and good interconnection, thus forming high-quality reservoirs. Cs, Ms, and Fs lithofacies have experienced relatively strong compaction, weak dissolution, and strong cementation, particularly because of the high clay mineral content, which significantly reduces the pore radius and blocks the throat, forming a large number of D-intraGs and InterCs. This results in poor connectivity and strong heterogeneity of pore structure, low movable fluid saturation, poor reservoir physical properties, and an easily formed dry layer. Therefore, pebbly coarse-grained sandstone and sandy conglomerate reservoirs with high quartz content should be regarded as the focus of gas field development.

6. Conclusions

The pore throat heterogeneity of distinct lithofacies of gravelly braided river deposits in the Lower Shihezi formation, northern Ordos Basin, has been thoroughly studied, as also the effect of diagenetic alteration on pore throat heterogeneity. The pore throat structure, physical properties, and diagenetic strength of various lithofacies are significantly distinct. Fine-grained sandstone (Fs), medium-grained sandstone (Ms), coarse-grained sandstone (Cs), sandy conglomerate (Sc), and pebbled coarse-grained sandstone (Ps) exhibit gradually improving physical properties. In the lithofacies with the coarser grain size, the larger the pore throat radius, which mainly contributes to the permeability, the larger the average throat radius and the pore throat coordination number, the higher the movable fluid saturation. Moreover, the fractal dimensions D_l and D_s of lithofacies with coarser grain

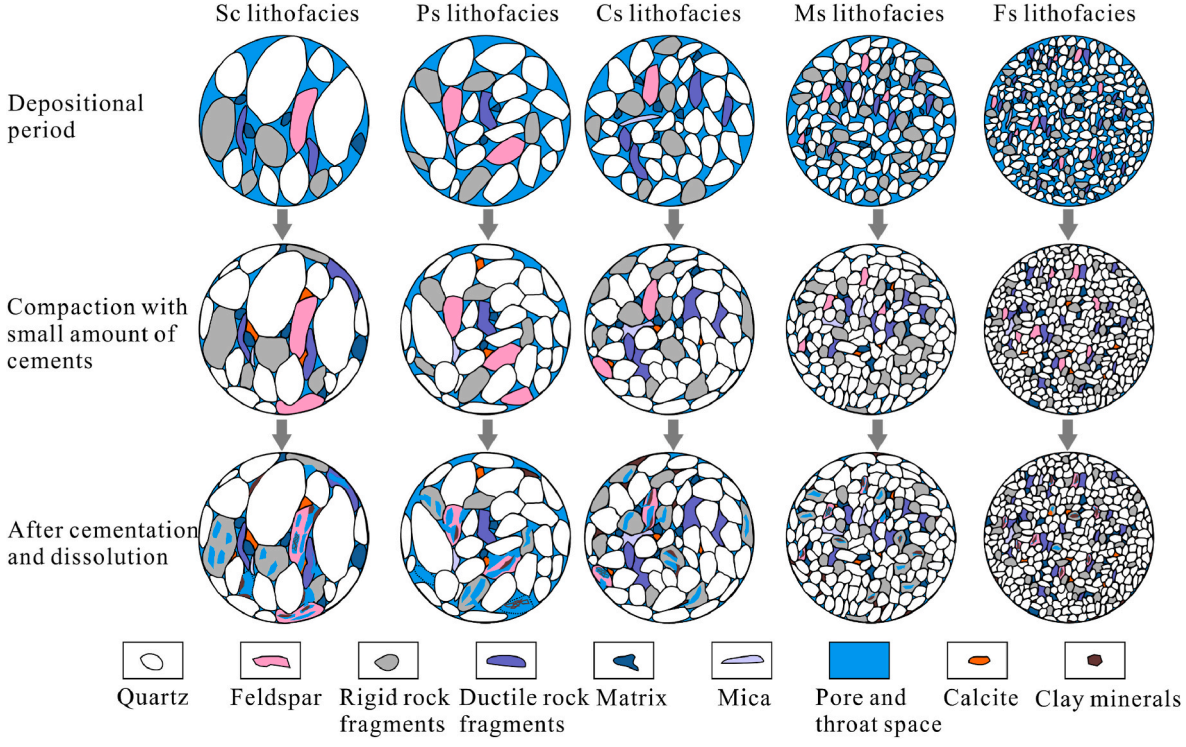

Fig. 23. Evolution model of the pore structure of different lithofacies in the Lower Shihezi formation reservoir.

sizes are smaller, indicating that the pore throat structure is more homogeneous. Strong compaction and cementation of calcite and clay minerals are the main factors leading to the reservoir quality degradation of the Lower Shihezi formation. Secondary dissolution pores account for 80% of the average total surface porosity, particularly D-InterGs and MP, which effectively improve the reservoir quality. The Ps and Sc lithofacies have undergone relatively weak compaction and strong dissolution, possess more R-interGs, D-interGs, and MP, and contain fewer clay minerals, so they have the greatest reservoir quality. The Fs reservoir is characterized by strong compaction, low primary pore content, and high clay mineral content. It is difficult for acidic fluid to enter the narrow pore space, and it is easy to form D-intraGs and InterCs. So, the Fs reservoir has poor pore throat connectivity, strong heterogeneity, and the worst reservoir quality. Although early calcite cement can resist compaction and provide a material basis for dissolution, overall calcite content has a negative effect on reservoir quality. Filamentous illite in clay minerals obstructs the throat and causes the most substantial damage to pore throat size and connectivity. Because Ps and Sc lithofacies have undergone relatively weak compaction, strong dissolution, and weak cementation, they are considered high-quality reservoirs in the Lower Shihezi formation. The formation mechanism of different types of clay minerals in various lithofacies of coarse-grained tight sandstone reservoirs and their influence on reservoir quality need further study.

Credit author statement

Dingding Zhao: Conceptualization, Methodology, Software, Investigation, Writing-Original Draft. **Jiagen Hou:** Supervision, Writing – Review & Editing. **Hemanta Sarma:** Methodology, Writing – Review & Editing. **Wenjie Guo:** Software, Data Curation. **Yuming Liu:** Supervision, Investigation. **Pengfei Xie:** Software, Review & Editing. **Luxing Dou:** Methodology, Investigation. **Ruxian Chen:** Software. **Zhanyang Zhang:** Investigation.

Declaration of competing interest

The authors declare that they have no known competing financial interests or personal relationships that could have appeared to influence the work reported in this paper.

Data availability

The authors do not have permission to share data.

Acknowledgements

We appreciate the geologists from the North China Company, SINOPEC for providing cores samples and test data. This work was supported by China Scholarship Council (CSC File No.202106440047).

References

Aliyev, E., Saidian, M., Prasad, M., Russell, B., 2016. Rock typing of tight gas sands: a case study in Lance and Mesaverde formations from Jonah field. J. Nat. Gas Sci. Eng. 33, 1260–1270.
Arnott, R.W.C., 2003. The role of fluid- and sediment-gravity flow processes during deposition of deltaic conglomerates (Cardium Formation, Upper Cretaceous), west-central Alberta. Bull. Can. Petrol. Geol. 51, 426–436.
Bai, D., Yang, M., Lei, Z., Zhang, Y., 2020. Effect of tectonic evolution on hydrocarbon charging time: a case study from Lower Shihezi Formation (Guadalupian), the Hangjinqi area, northern Ordos, China. J. Petrol. Sci. Eng. 184, 106465.
Barth, T., Bjørlykke, K., 1993. Organic acids from source rock maturation: generation potentials, transport mechanisms and relevance for mineral diagenesis. Appl. Geochem. 8 (4), 325–337.
Bjørlykke, K., 2014. Relationships between depositional environments, burial history and rock properties. Some principal aspects of diagenetic process in sedimentary basins. Sediment. Geol. 301, 1–14.
Bluck, B., 1979. Structure of coarse grained braided stream alluvium. Earth Environ. Sci. Trans. R. Soc. Edinburgh 70 (10–12), 181–221.
Broseta, D., Barre, L., Vizika, O., Shahidzadeh, N., Guilbaud, J.P., Lyonnard, S., 2001. Capillary condensation in a fractal porous medium. Phys. Rev. Lett. 86, 5313–5316.
Cant, D.J., Ethier, V.G., 1984. Lithology-dependent diagenetic control of reservoir properties of conglomerates, Falher member, Elmworth field, Alberta. AAPG Bull. 68 (8), 1044–1054.
Cao, B., Sun, W., Li, J., 2021. Reservoir petrofacies — a tool for characterization of reservoir quality and pore structures in a tight sandstone reservoir: a study from the sixth member of Upper Triassic Yanchang Formation, Ordos Basin, China. J. Petrol. Sci. Eng. 199, 108294.
Cook, J.E., Goodwin, L.B., Boutt, D.F., 2011. Systematic diagenetic changes in the grain-scale morphology and permeability of a quartz-cemented quartz arenite. AAPG Bull. 95 (6), 1067–1088.
Dai, J.X., Li, J., Luo, X., Zhang, W.Z., Hu, G.Y., , M, C.H., Guo, J.M., Ge, S.G., 2005. Stable carbon isotope compositions and source rock geochemistry of the giant gas accumulations in the Ordos Basin. China. Org. Geochem. 36, 1617–1635.
Dai, J.X., Ni, Y.Y., Wu, X.Q., 2012. Tight gas in China and its significance in exploration and exploitation. Petrol. Explor. Dev. 39 (3), 277–284.
Daigle, H., Johnson, A., Thomas, B., 2014. Determining fractal dimension from nuclear magnetic resonance data in rocks with internal magnetic field gradients. Geophysics D425–D431.
Daigle, H., Johnson, A., 2016. Combining mercury intrusion and nuclear magnetic resonance measurements using percolation theory. Transport Porous Media 111, 669–679.
De Ros, L.F., Goldberg, K., 2007. Reservoir Petrofacies: A Tool for Quality Characterization and Prediction, AAPG Annual Convention. American Association of Petroleum Geologists, Long Beach, California.
Dixon, S.A., Summers, D.M., Surdam, R.C., 1989. Diagenesis and preservation of porosity in Norphlet formation (upper Jurassic), southern Alabama. AAPG Bull. 77, 707–728.
Dong, H., Blunt, M.J., 2009. Pore-network extraction from micro-computerized tomography images. Phys. Rev. E 80 (3), 036307.
Dutton, S.P., 2008. Calcite cement in Permian deep-water sandstones, Delaware Basin west Texas: origin, distribution, and effect on reservoir properties. AAPG Bull. 92 (6), 765–787.
Ebinghaus, A., McCann, T., Augustsson, C., 2012. Facies and provenance analysis of Paleogene-age alluvial conglomerates from the northern part of the Mesta Basin, SW Bulgaria. Geol. J. 47, 409–425.
Ehrenberg, S.N., 1989. Assessing the relative importance of compaction processes and cementation to reduction of porosity in sandstones: discussion; compaction and porosity evolution of pliocene sandstones, ventura basin, California: Discussion. AAPG Bull. 73, 1274–1276.
El-ghali, M.A.K., Tajori, K.G., Mansurbeg, H., Ogle, N., Kalin, R.M., 2006. Origin and timing of siderite cementation in Upper Ordovician glaciogenic sandstones from the Murzuq basin, SW Libya. Mar. Petrol. Geol. 23 (4), 459–471.
Fan, A., Yang, R., Lenhardt, N., Wang, M., Han, Z., Li, J., Li, Y., Zhao, Z., 2019. Cementation and porosity evolution of tight sandstone reservoirs in the Permian Sulige gas field, Ordos Basin (central China). Mar. Petrol. Geol. 103, 276–293.
Fawad, M., Mondol, N.H., Jahren, J., Bjørlykke, K., 2011. Mechanical compaction and ultrasonic velocity of sands with different texture and mineralogical composition. Geophys. Prospect. 59 (4), 697–720.
Feng, C., Melnyk, S., Ross, C., Shanley, K., Zonneveld, J., Gingras, M.K., 2021. Lithofacies-dependent pore-throat radii and reservoir properties in the lower triassic montney formation, Puskwaskau field, alberta. Mar. Petrol. Geol. 131, 105157.
Folk, R.L., Andrews, P.B., Lewis, D.W., 1970. Detrital sedimentary rock classification and nomenclature for use in New Zealand. N. Z. J. Geol. Geophys. 13, 937–968.
Gao, J., Ma, B., Lu, Y., Zhang, W., Cao, Q., 2022. Origin of authigenic kaolinite with implications for Permian tight gas sandstone reservoirs in the northern Ordos Basin, central China. J. Nat. Gas Sci. Eng. 99, 104429.
Guo, X., Huang, Z., Zhao, L., Han, W., Ding, C., Sun, X., Yan, R., Zhang, T., Yang, X., Wang, R., 2019. Pore structure and multi-fractal analysis of tight sandstone using MIP, NMR and NMRC methods: a case study from the Kuqa depression, China. J. Pet. Sci. Eng. 178, 544–558.
Haile, B.G., Klausen, T.G., Czarniecka, U., Xi, K., Jahren, J., Hellevang, H., 2018. How are diagenesis and reservoir quality linked to depositional facies? A deltaic succession, Edgeøya, Svalbard. Mar. Petrol. Geol. 92, 519–546.
He, F., Wang, F., Zhang, W., An, C., Qi, R., Ma, C., Chen, Y., Li, C., Fan, L., Gui, P., 2020. Transformation of exploration ideas and a major breakthrough in natural gas exploration in the northern margin of the Ordos Basin. China Pet. Explor. 25 (6), 39–49 (in Chinese with English abstract).
Heward, A.P., 1989. Early Ordovician alluvial fan deposits of the Marmul oil field, South Oman. J. Geol. Soc. London. 146, 557–565.
Higgs, K.E., Zwingmann, H., Reyes, A.G., Funnell, R.H., 2007. Diagenesis, porosity evolution, and petroleum emplacement in tight gas reservoirs, Taranaki basin, New Zealand. J. Sediment. Res. 77, 1003–1025.
Huang, H., Li, R., Jiang, Z., Li, J., Chen, L., 2020a. Investigation of variation in shale gas adsorption capacity with burial depth: insights from the adsorption potential theory. J. Nat. Gas Sci. Eng. 73, 103043.
Huang, H., Li, R., Xiong, F., Hu, H., Sun, W., Jiang, Z., Chen, L., Wu, L., 2020b. A method to probe the pore-throat structure of tight reservoirs based on low-field NMR: insights from a cylindrical pore model. Mar. Petrol. Geol. 117, 104344.
Jia, A., He, D., Wei, Y., Li, Y., 2021. Predictions on natural gas development trend in China for the next fifteen years. J. Nat. Gas Geosci. 6 (2), 67–78.
Katz, A.J., Thompson, A.H., 1985. Fractal sandstone pores: implications for conductivity and pore formation. Phys. Rev. Lett. 54, 1325–1328.
Lai, J., Wang, G., 2015. Fractal analysis of tight gas sandstones using high-pressure mercury intrusion techniques. J. Nat. Gas Sci. Eng. 24, 185–196.

Lai, J., Wang, G., Cao, J., Xiao, C., Wang, S., Pang, X., Dai, Q., He, Z., Fan, X., Yang, L., Qin, Z., 2018a. Investigation of pore structure and petrophysical property in tight sandstones. Mar. Petrol. Geol. 91, 179–189.
Lai, J., Wang, G., Fan, Z., Zhou, Z., Chen, J., Wang, S., 2018b. Fractal analysis of tight shaly sandstones using nuclear magnetic resonance measurements. AAPG Bull. 102 (2), 175–193.
Li, K., 2010. Analytical derivation of Brooks-Corey type capillary pressure models using fractal geometry and evaluation of rock heterogeneity. J. Pet. Sci. Eng. 73 (1–2), 20–26.
Li, J., Zhang, J., Liu, S., Fan, Z., Xue, H., 2016. Sedimentology and sequence stratigraphy of the paleogene lower second member of the shahejie formation, W79 block, wenliu oilfield, bohai bay basin, China. Russ. Geol. Geophys. 57, 944–957.
Li, M., Guo, Y., Li, Z., Wang, H., 2020a. The diagenetic controls of the reservoir heterogeneity in the tight sand gas reservoirs of the Zizhou Area in China's east Ordos Basin: implications for reservoir quality predictions. Mar. Petrol. Geol. 112, 104088.
Li, Y., Xu, W., Wu, P., Meng, S., 2020b. Dissolution versus cementation and its role in determining tight sandstone quality: a case study from the Upper Paleozoic in northeastern Ordos Basin, China. J. Nat. Gas Sci. Eng. 78, 103324.
Li, J., Zhang, X., Tian, J., Liang, Q., Cao, T., 2021. Effects of deposition and diagenesis on sandstone reservoir quality: a case study of Permian sandstones formed in a braided river sedimentary system, northern Ordos Basin, Northern China. J. Asian Earth Sci. 213, 104745.
Liu, Q., Jin, Z., Meng, Q., Wu, X., Jia, H., 2015. Genetic types of natural gas and filling patterns in Daniudi gas field, Ordos Basin, China. J. Asian Earth Sci. 107, 1–11.
Liu, Y., Hu, W., Cao, J., Wang, X., Tang, Q., 2018. Diagenetic constraints on the heterogeneity of tight sandstone reservoirs: a case study on the Upper Triassic xujiahe formation in the Sichuan basin, southwest China. Mar. Petrol. Geol. 92, 650–669.
Lunt, I.A., Bridge, J.S., 2004. Evolution and deposits of a gravelly braid bar, Sagavanirktok River, Alaska. Sedimentology 51 (3), 415–432.
Mao, Z., He, Y., Ren, X., 2005. An improved method of using NMR T2 distribution to evaluate pore size distribution. Chin. J. Geophys. 48 (2), 412–418.
Mahmic, O., Dypvik, H., Hammer, E., 2018. Diagenetic influence on reservoir quality evolution, examples from Triassic conglomerates/arenites in the Edvard Grieg field, Norwegian North Sea. Mar. Petrol. Geol. 93, 247–271.
Mandelbrot, B.B., 1975. Les objets fractals: forme, hasard et dimension. Flammarion, Paris.
Meadows, N., Beach, A., 1993. Controls on Reservoir Quality in the Triassic Sherwood Sandstone of the Irish Sea. Geological Society of London, Petroleum Geology Conference Series, pp. 823–833.
Mehrabi, H., Esrafili-Dizaji, B., Hajikazemi, E., Noori, B., Mohammad-Rezaei, H., 2019. Reservoir characterization of the Burgan Formation in northwestern Persian gulf. J. Petrol. Sci. Eng. 174, 328–350.
Miall, A.D., 1977. A review of the braided-river depositional environment. Earth Sci. Rev. 13 (1), 1–62.
Misiak, B.U., Przybycin, A., Winid, B., 2014. Shale and tight gas in Poland-legal and environment issues. Energy Pol. 65, 68–77.
Nie, R., Zhou, J., Chen, Z., Liu, J., Pan, Y., 2021. Pore structure characterization of tight sandstones via a novel integrated method: a case study of the Sulige gas field, Ordos Basin (Northern China). J. Asian Earth Sci. 213, 104739.
Oluwadebi, A.G., Taylor, K.G., Dowey, P.J., 2018. Diagenetic controls on the reservoir quality of the tight gas Collyhurst sandstone formation, Lower Permian, East Irish Sea basin. United Kingdom. Sediment. Geol. 371, 55–74.
Pittman, E.D., Larese, R.E., 1991. Compaction of lithic sands: experimental results and applications. AAPG Bull. 75 (8), 1279–1299.
Qiao, J., Zeng, J., Jiang, S., Feng, S., Feng, X., Guo, Z., Teng, J., 2019. Heterogeneity of reservoir quality and gas accumulation in tight sandstone reservoirs revealed by pore structure characterization and physical simulation. Fuel 253, 1300–1316.
Qiao, J., Zeng, J., Jiang, S., Zhang, Y., Feng, S., Feng, X., Hu, H., 2020a. Insights into the pore structure and implications for fluid flow capacity of tight gas sandstone: a case study in the upper paleozoic of the Ordos Basin. Mar. Petrol. Geol. 118, 104439.
Qiao, J., Zeng, J., Jiang, S., Wang, Y., 2020b. Impacts of sedimentology and diagenesis on pore structure and reservoir quality in tight oil sandstone reservoirs: implications for macroscopic and microscopic heterogeneities. Mar. Petrol. Geol. 111, 279–300.
Qiao, J., Zeng, J., Cai, J., Jiang, S., An, T., Xiao, E., Zhang, Y., Feng, X., Yang, G., 2021. Pore-scale heterogeneity of tight gas sandstone: Origins and impacts. J. Nat. Gas Sci. Eng. 96, 104248.
Qin, S., Wang, R., Shi, W., Liu, K., Zhang, W., Xu, X., Qi, R., Yi, Z., 2022. Diverse effects of intragranular fractures on reservoir properties, diagenesis, and gas migration: Insight from Permian tight sandstone in the Hangjinqi area, north Ordos Basin. Mar. Petrol. Geol. 137, 105526.
Qu, Y., Sun, W., Tao, R., Luo, B., Chen, L., Ren, D., 2020. Pore–throat structure and fractal characteristics of tight sandstones in Yanchang Formation, Ordos Basin. Mar. Petrol. Geol. 120, 104573.
Rezaee, R., Saeedi, A., Clennell, B., 2012. Tight gas sands permeability estimation from mercury injection capillary pressure and nuclear magnetic resonance data. J. Petrol. Sci. Eng. 88, 92–99.
Saidian, M., Prasad, M., 2015. Effect of mineralogy on nuclear magnetic resonance surface relaxivity: a case study of Middle Bakken and Three Forks fromations. Fuel 161, 197–206.
Schmid, S., Worden, R.H., Fisher, Q.J., 2004. Diagenesis and reservoir quality of the Sherwood sandstone (triassic), corrib field , Slyne basin, west of Ireland. Mar. Petrol. Geol. 21, 299–315.
Schmoker, J.W., Gautier, D.L., 1988. Sandstone porosity as a function of thermal maturity. Geology 16 (12), 1007–1010.
Spencer, C.W., 1989. Review of characteristics of low-permeability gas reservoirs in western United States. AAPG Bull. 73 (5), 613–629.
Stroker, T.M., Harris, N.B., Elliott, W.C., Wampler, J.M., 2013. Diagenesis of a tight gas sand reservoir: upper cretaceous mesaverde group, Piceance basin, Colorado. Mar. Petrol. Geol. 40, 48–68.
Sun, L., Zou, C., Jia, A., Wei, Y., Zhu, R., Wu, S., Guo, Z., 2019. Development characteristics and orientation of tight oil and gas in China. Petrol. Explor. Dev. 46 (6), 1073–1087.
Surdam, R.C., Crossly, L.J., Hagen, E.S., Heasler, H.P., 1989. Organic-inorganic interactions and sandstone diagenesis. AAPG Bull. 73, 1–23.
Taylor, T.R., Giles, M.R., Hathon, L.A., Diggs, T.N., Braunsdorf, N.R., Birbiglia, G.V., Kittridge, M.G., Macaulay, C.I., Espejo, I.S., 2010. Sandstone diagenesis and reservoir quality prediction: models, myths, and reality. AAPG Bull. 94 (8), 1093–1132.
Taylor, K.G., Machent, P.G., 2011. Extensive carbonate cementation of fluvial sandstones: an integrated outcrop and petrographic analysis from the Upper Cretaceous, Book Cliffs, Utah. Mar. Petrol. Geol. 28 (8), 1461–1474.
Tobin, R.C., McClain, T., Lieber, R.B., Ozkan, A., Banfield, L.A., Marchand, A.M.E., McRae, L.E., 2010. Reservoir quality modeling of tight-gas sands in Wamsutter field: integration of diagenesis, petroleum systems, and production data. AAPG Bull. 94, 1229–1266.
Tong, X., Guo, B., Li, J., Huang, F., 2012. Comparison study on accumulation & distribution of tight sandstone gas between China and the United States and its significance. Eng. Sci. 14 (6), 9–15 (in Chinese with English abstract).
Wang, T., Hou, M.C., Chen, H.D., Hou, Z.J., Chen, A.Q., Su, Z.T., 2014. Coupling relationship between Yinshan episodic orogenic movement of Hercynian tectonic cycle and filing cycle of the North Ordos Basin in China. J. Chengdu Univ. Technol. (Sci. Technol. Ed.) 41, 310–317 (in Chinese with English abstract).
Wang, W., Yue, D., Zhao, J., Li, W., Wang, B., Wu, S., Li, S., 2019. Diagenetic alteration and its control on reservoir quality of tight sandstones in lacustrine deep-water gravity-flow deposits; a case study of the Yanchang Formation, southern Ordos Basin, China. Mar. Petrol. Geol. 110, 676–694.
Wang, R., Shi, W., Xie, X., Zhang, W., Qin, S., Liu, K., Busbey, A.B., 2020a. Clay mineral content, type, and their effects on pore throat structure and reservoir properties: Insight from the Permian tight sandstones in the Hangjinqi area, north Ordos Basin, China. Mar. Petrol. Geol. 115, 104281.
Wang, X., Hou, J., Li, S., Dou, L., Song, S., Kang, Q., Wang, D., 2020b. Insight into the nanoscale pore structure of organic-rich shales in the Bakken Formation, USA. J. Pet. Sci. Eng. 191, 107182.
Wang, Q., Chen, D., Gao, X., Wang, F., Li, J., Liao, W., Wang, Z., Xie, G., 2020c. Microscopic pore structures of tight sandstone reservoirs and their diagenetic controls: a case study of the Upper Triassic Xujiahe Formation of the Western Sichuan Depression, China. Mar. Petrol. Geol. 113, 104119.
Wang, X., Zhang, F., Li, S., Dou, L., Liu, Y., Ren, X., Chen, D., Zhao, W., 2021a. The architectural surfaces characteristics of sandy braided river reservoirs, case study in gudong oil field, China. Geofluids 1–12.
Wang, G., Zhu, R., Zheng, X., Hu, J., Wang, Z., Shi, X., 2021b. Characterization and genetic significance of mold pores in tight sandstone: a case from the lower part of the Yanchang Formation in the Wuqi–Ansai area. Mar. Petrol. Geol. 124, 104790.
Wheatley, D., Hollingworth, S., Steele, P., Chan, M., 2020. Sedimentology, diagenesis, and reservoir characterization of the Permian White Rim Sandstone, southern Utah: implications for carbon capture and sequestration potential. AAPG Bull. 104 (6), 1357–1373.
Wilkinson, M., Darby, D., Haszeldine, R.S., Couples, G.D., 1997. Secondary porosity generation during deep burial associated with overpressure leak-off: fulmar Formation, United Kingdom Central Graben. AAPG Bull. 81 (5), 803–813.
Wilson, R.D., Chitale, J., Huffman, K., Montgomery, P., Prochnow, S.J., 2020. Evaluating the depositional environment, lithofacies variation, and diagenetic processes of the Wolfcamp B and lower Spraberry intervals in the Midland Basin: implications for reservoir quality and distribution. AAPG Bull. 104 (6), 1287–1321.
Worden, R.H., Morad, S., 2003. Clay minerals in sandstones: a review of the detrital and diagenetic sources and evolution during burial. In: International Association of Sedimentologists. Special Publication 34, pp. 3–41.
Wu, Y., Tahmasebi, P., Lin, C., Zahid, M.A., Dong, C., Golab, A.N., Ren, L., 2019. A comprehensive study on geometric, topological and fractal characterizations of pore systems in low-permeability reservoirs based on SEM, MICP, NMR, and X-ray CT experiments. Mar. Petrol. Geol. 103, 12–28.
Xiao, X., Zhao, B., Thu, Z., Song, Z., Wilkins, R., 2005. Upper paleozoic petroleum system, Ordos basin, China. Mar. Petrol. Geol. 22, 945–963.
Xiao, M., Wu, S., Yuan, X., Cao, Z., Xie, Z., 2020. Diagenesis effects on the conglomerate reservoir quality of the Baikouquan formation, Junggar Basin, China. J. Petrol. Sci. Eng. 195, 107599.
Xu, Q., Shi, W., Xie, X., Busbey, A.B., Xu, L., Wu, R., Liu, K., 2018. Inversion and propagation of the late paleozoic Porjianghaizi fault (north Ordos Basin, China): controls on sedimentation and gas accumulations. Mar. Petrol. Geol. 91, 706–722.
Yang, H., Zhang, J., Wang, F.Y., Wang, H.C., 2000. Characteristics of Paleozoic gas system in E'erduosi Basin. Nat. Gas. Ind. 20, 7–11.
Yang, Y.T., Li, W., Ma, L., 2005. Tectonic and stratigraphic controls of hydrocarbon systems in the Ordos basin: a multicycle cratonic basin in central China. AAPG Bull. 89, 255–269.
Yang, H., Fu, J., Liu, X., Meng, P., 2012. Accumulation conditions and exploration and development of tight gas in the Upper Paleozoic of the Ordos Basin. Petrol. Explor. Dev. 39 (3), 315–324.
Yang, W., Hou, J., Liu, Y., Dou, L., Wang, X., 2022. The pore structures of different lithofacies in low-permeability sandy conglomerate reservoirs and their diagenetic

impacts: a case study from the Es4 member of the northern steep slope in Dongying Depression, Bohai Bay Basin, NE China. Mar. Petrol. Geol. 136, 105481.
Yin, S., Dong, L., Yang, X., Wang, R., 2020. Experimental investigation of the petrophysical properties, minerals, elements and pore structures in tight sandstones. J. Nat. Gas Sci. Eng. 76, 103189.
Yu, Y., Lin, L., Zhai, C., Chen, H., Wang, Y., Li, Y., Deng, X., 2019. Impacts of lithologic characteristics and diagenesis on reservoir quality of the 4th member of the Upper Triassic Xujiahe Formation tight gas sandstones in the western Sichuan Basin, southwest China. Mar. Petrol. Geol. 107, 1–19.
Zhang, C., Chen, Z., Zhang, Z., Li, J., Ling, H., Sun, B., 2007. Fractal characteristics of reservoir rock pore structure based on NMR T2 distribution. J. Oil Gas Technol. (J. Jianghan Petroleum Inst.) 29 (4), 80–86.
Zhang, P., Zhang, J., Wang, J., Li, M., Liang, J., 2018. Flow units classification for geostatisitical three-dimensional modeling of a non-marine sandstone reservoir: a case study from the Paleocene Funing Formation of the Gaoji Oilfield, east China. Open Geosci. 10, 113–120.
Zhang, F., Jiang, Z., Sun, W., Li, Y., Zhang, X., Zhu, L., Wen, M., 2019. A multiscale comprehensive study on pore structure of tight sandstone reservoir realized by nuclear magnetic resonance, high pressure mercury injection and constant-rate mercury injection penetration test. Mar. Petrol. Geol. 109, 208–222.
Zhang, F., Jiang, Z., Xiao, H., Hu, B., Chen, P., Tang, X., Sun, W., Zhu, L., Wang, Q., 2022. Testing origin of reservoir quality difference of tight sandstones in the Yanchang Formation, Ordos Basin, China. Mar. Petrol. Geol. 137, 105507.
Zhang, J., Liu, G., Torsaeter, O., Tao, S., Jiang, M., Li, G., Zhang, S., 2020. Pore-throat structure characteristics and its effect on flow behavior in Gaotaizi tight siltstone reservoir, northern Songliao Basin. Mar. Petrol. Geol. 122, 104651.
Zheng, J., Ying, F., 1997. Reservoir characteristics and diagenetic model of sandstone intercalated in coal-bearing strata (acid water medium). Acta Pet. Sin. 18 (4), 19–24 (in Chinese with English abstract).
Zheng, Q., Yu, B., 2012. A fractal permeability model for gas flow through dual-porosity media. J. Appl. Phys. 111, 024316.
Zheng, D., Pang, X., Jiang, F., Liu, T., Shao, X., Huyan, Y., 2020. Characteristics and controlling factors of tight sandstone gas reservoirs in the Upper Paleozoic strata of Linxing area in the Ordos Basin, China. J. Nat. Gas Sci. Eng. 75, 103135.
Zhu, F., Hu, W., Cao, J., Sun, F., Liu, Y., Sun, Z., 2018. Micro/nanoscale pore structure and fractal characteristics of tight gas sandstone: a case study from the Yuanba area, northeast Sichuan Basin, China. Mar. Petrol. Geol. 98, 116–132.
Zou, C., Zhang, G., Yang, Z., Tao, S., Hou, L., Zhu, R., Yuan, X., Ran, Q., Li, D., Wang, Z., 2013. Concepts, characteristics, potential and technology of unconventional hydrocarbons: on unconventional petroleum geology. Petrol. Explor. Dev. 40 (4), 413–428.
Zou, C., Yang, Z., He, D., Wei, Y., Li, J., Jia, A., Chen, J., Zhao, Q., Li, Y., Li, J., Yang, S., 2018. Theory, technology and prospects of conventional and unconventional natural gas. Petrol. Explor. Dev. 45 (4), 575–587.